J. Fluid Mech. (2004), vol. 502, pp. 233–271. © 2004 Cambridge University Press
DOI: 10.1017/S0022112003007419 Printed in the United Kingdom

Experimental investigation of Rayleigh–Taylor mixing at small Atwood numbers

By P. RAMAPRABHU AND M. J. ANDREWS†
Department of Mechanical Engineering, Texas A&M University, College Station, TX 77843, USA

(Received 28 April 2003 and in revised form 19 September 2003)

The self-similar evolution to turbulence of a multi-mode Rayleigh–Taylor mix at small density differences ($A_t \sim 7.5 \times 10^{-4}$), is investigated through particle image velocimetry (PIV), and high-resolution thermocouple measurements. The density difference has been achieved through a temperature difference in the fluid. Cold fluid enters above the hot in a closed channel to form an unstable interface. This buoyancy-driven mixing experiment allows for long data collection times, short transients, and is statistically steady. First-, second-, and third-order statistics with spectra of velocity and temperature fields are presented. Analysis of the measurements has shed light on the structure of mixing as it develops to a self-similar regime in this flow. The onset of self-similarity is marked by the development of a self-preserving form of the temperature spectra, and the collapse of velocity profiles expressed in self-similar units. Vertical velocity fluctuations dominate horizontal velocity fluctuations in this experiment, with a ratio approaching 2:1 in the self-similar regime. This anisotropy extends to the Taylor microscales that undergo differential straining in the direction of gravity. Up to two decades of velocity spectra development, and four decades of temperature spectra, have been captured from the experiment. The velocity spectra consist of an inertial range comprised of anisotropic vertical and horizontal velocity fluctuations, and a more isotropic dissipative range. Buoyancy forcing occurs across the spectrum of velocity and temperature scales, but was not found to affect the structure of the spectra, resulting in a $-5/3$ slope, similar to other canonical turbulent flows. A scaling argument is presented to explain this observation. The net kinetic energy dissipation, as the flow evolves from an initial state to a final self-similar state was measured to be 49% of the accompanying loss in potential energy, and is in close agreement with values obtained from three-dimensional numerical simulations.

1. Introduction

Rayleigh–Taylor (R-T) instability is induced when a density gradient is accelerated, in the presence of infinitesimal perturbations, by a pressure gradient in the opposite direction such that $\nabla p \cdot \nabla \rho < 0$ (Chandrasekhar 1961). If the initial density interface comprises a spectrum of velocity and/or density disturbances, then the pressure gradient drives the growth of the perturbation to form a mix region whose width grows in time. Development of the mix was divided by Youngs (1984) into three successive regimes: (i) initially an exponential growth of infinitesimal perturbations that

---

† Author to whom correspondence should be addressed: mandrews@mengr.tamu.edu

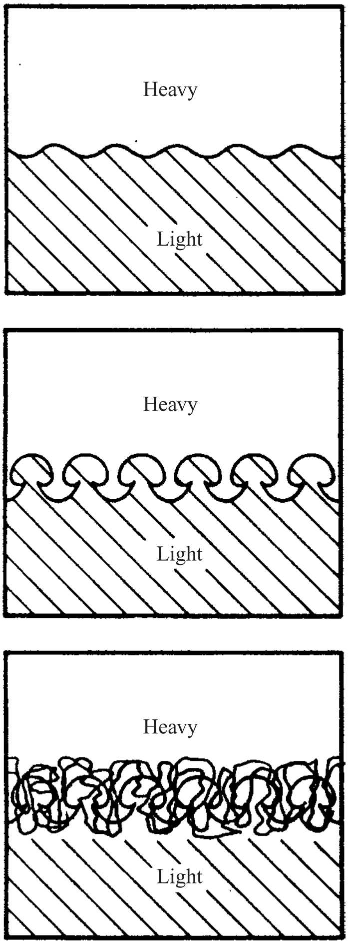

FIGURE 1. Stages of the evolution of R-T instability.

correspond to linear stability analysis; (ii) at amplitudes of about half the wavelength, the instability saturates and the perturbation speed grows at a constant rate; and (iii) thereafter, longer wavelengths overtake owing to their continuing growth. Emmons, Chang & Watson (1960) coined the term 'bubble competition' to describe this last regime. Eventually, through mode interaction and successive wavelength saturation, a self-similar R-T mix layer is formed (figure 1). To illustrate the mixing process, figure 2 shows planar laser induced fluorescence (PLIF) photographs taken from the experiment described herein. The fluid is water, with the top layer at a temperature of 17 °C and the bottom layer at 22 °C, and the flow direction is from left to right. The temperature difference provides a corresponding small density difference due to thermal expansion. Inspection of the photographs reveals that at early times (figure 2*a*) as the two streams leave the edge of a splitter plate, two-dimensional single-wavelength perturbations can be seen growing downstream. The leaning of early-time structures is due to the development of boundary layers on the splitter plate. From the mean velocity profiles immediately after the splitter plate, the associated velocity deficit was estimated to be $\sim 0.4\,\mathrm{cm\,s^{-1}}$ ($\sim 10\%$ of the mean convective velocity). However, this velocity defect is neutralized rapidly (by $x \sim 2\,\mathrm{cm}$)

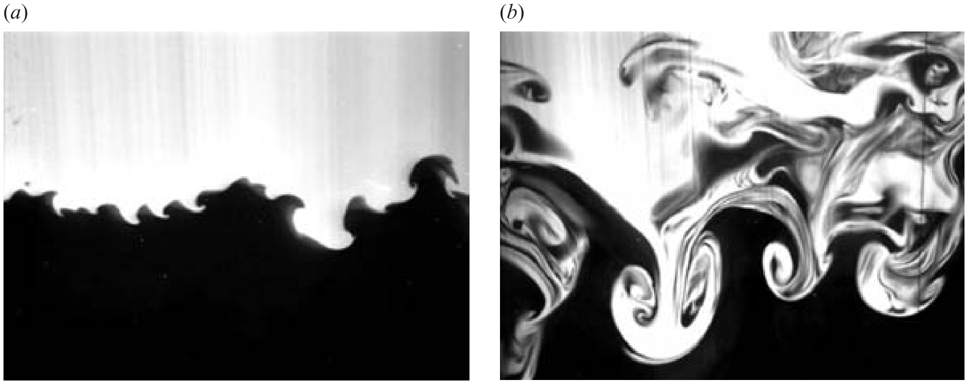

FIGURE 2. Planar laser induced fluorescence (PLIF) images at (*a*) early and (*b*) late times of the evolution of the R-T instability.

due to the buoyancy-driven vertical transport of momentum and due to diffusion (Ramaprabhu 2003). This is in contrast with late-time complex vortical structures (figure 2*b*), which show streaks of darker fluid trapped fully inside the lighter fluid. This can only occur if there is significant three-dimensionality that results in out-of-plane fluid being entrained into the plane of visualization. At these late times, single-wavelength perturbations have interacted and developed into larger scales in the process described by Youngs (1984). The nonlinearity at late time is evident from the presence of a wide range of scales not seen in figure 2(*a*). The bubbles seen at late time are travelling downward with a terminal velocity defined below. The mushroom-shaped structures in figure 2(*b*) are typical of R-T mixing layers. Figure 2(*b*) also shows many secondary roll-up processes, especially on the large inverted mushroom, slightly to the left of the vertical centreline. Often these secondary roll-ups are driven by shear resulting in a localized Kelvin–Helmholtz instability. We return to this mixing process for a detailed investigation later in the paper.

Once at self-similarity, dimensional analysis (Youngs 1984) shows the half-mix-width h, must grow quadratically with time according to:

$$h = \alpha A_t g t^2, \tag{1}$$

where A_t, the Atwood number is the governing parameter of the flow defined by $A_t = (\rho_1 - \rho_2)/(\rho_1 + \rho_2)$, ρ_1 and ρ_2 are the cold- and hot-water densities employed in the present work, g is the acceleration due to gravity, and α is a constant. For large $A_t \to 1$ (as $\rho_1/\rho_2 \to \infty$), the mix is no longer symmetric about the density interface, then h corresponds to the bubble penetration distance from the position of the initial unstable interface.

Equation (1) for h was arrived at by Youngs (1984) through a nonlinear extension of the linear stability theory (Chandrasekhar 1961). In the linear regime, assuming the viscous forces are negligible, the growth rate of the most dominant mode is given by (Youngs 1984)

$$n_m = \left\{ \frac{\pi g}{l_m} \frac{\rho_1 - \rho_2}{\rho_1 + \rho_2} \right\}^{1/2}, \tag{2}$$

where l_m is the dominant wavelength. In the nonlinear regime, the width of the mix may be taken as being proportional to the dominant wavelength (Lewis 1950), and $h \sim l_m$. If the dominant mode takes N exponential turnover times to evolve, then

$n_m t = N$. Thus, solving (2) for l_m, the mix width is given by

$$h \propto l_m = \frac{2\pi}{N^2} \frac{\rho_1 - \rho_2}{\rho_1 + \rho_2} g t^2. \tag{3}$$

This argument is similar to the 'e^{10}' approach for describing the transition of Tolmien–Schlichting waves in a boundary layer (Jaffe, Okamura & Smith 1970). Indeed, coincidentally, Youngs (1984) suggests taking $N = 10$ (i.e. 10 exponential turnover times). This gives an estimate for α as $2\pi/N^2 \sim 0.06$. Another approach is to employ the terminal velocity for a dominant wavelength (bubble), given by $v_\infty = c_\infty \sqrt{(\rho_1 - \rho_2/\rho_1) g R_b}$ where R_b is the bubble radius (Daly 1967; Ratafia 1973). Daly also suggests the use of $D_b \sim \lambda_b = l_m \rho_1/(\rho_1 + \rho_2)$ to characterize the dependence of spike and bubble diameters on the wavelength and density ratio ρ_1/ρ_2, i.e. at high density ratios ($A_t \to 1$), the spikes are very narrow and $D_b = l_m$. At low density ratios, spikes and bubbles have nearly equal diameters given by $D_b = l_m/2$. Substituting for $R_b = D_b/2$ in the above expression for bubble terminal velocity, we obtain $v_\infty = c_\infty \sqrt{A_t g l_m/2}$. For low Atwood numbers ($\rho_1/\rho_2 = 1.1$), Daly (1967) found c_∞ to be ~ 0.7. Then, in the nonlinear regime, we can take $v_\infty = \mathrm{d}h/\mathrm{d}t = \mathrm{d}l_m/\mathrm{d}t$ giving upon integration over time, $l_m = \alpha A_t g t^2$ and $\alpha \sim 0.05$, using $h \sim l_m$ and $h = 0$ at $t = 0$.

The implication of (1) is that at self-similarity all memory of the initial conditions has been lost, and the only relevant length scale is gt^2. While this suggests that α is a universal constant, experiments and numerical simulations have produced differing values. The value of α has been measured at ~ 0.03 from numerical simulations (Young *et al.* 2001; Youngs 1984), while experimental values are usually higher. Dalziel (1993), Snider & Andrews (1994) and Read (1984) report a value of 0.07 from their experiments, while the linear electric motor (LEM) experiments of Dimonte & Schneider (2000) give a value of 0.05. Glimm *et al.* (2001) use a front-tracking algorithm in their three-dimensional simulations that yield a value of 0.07 comparable with experiments. Linden, Redondo & Youngs (1994) report a value of 0.044 ± 0.005, after introducing a virtual origin to account for any transients that may be present owing to the initial withdrawal of the dividing plate in their experiment. The difference in the values of α between experiments and numerical simulations is believed to be due to the presence of long wavelengths in experiments, while most numerical simulations are initialized with short-wavelength content that evolve purely through mode-coupling (Cook & Dimotakis 2001; Young *et al.* 2001; Youngs 2003). When such long wavelengths are present, α is no longer universal, but depends (logarithmically) on the initial amplitudes. Conversely, in the mode-coupling limit present in most numerical simulations, α takes up a lower bound universal value (Dimonte 2004). Work is in progress elsewhere to resolve the differences between numerical simulations and experiments (Dimonte *et al.* 2004).

The buoyancy-driven instabilities described above appear in environmental flows such as effluent discharge into rivers and estuaries, and in industrial applications such as heat exchangers and sprays in internal combustors (Beale & Reitz 1999). Rayleigh–Taylor mixing also occurs during the implosion phase of the inertial confinement fusion process (Lindl 1998), which involves the high-power laser bombardment of a target fuel capsule. Target surface imperfections and non-uniformities in the beam provide initial perturbations for the R-T pressure-driven hydrodynamic instability. Here, turbulence-induced mixing sets an upper limit on the peak implosion velocity resulting in the reduction of yield, and it is of interest to dampen the growth of the instability in such cases. Perhaps the largest observable R-T mix is the finger-like ejecta of stellar material believed to be present in the remnants of a young supernova (Gull 1975).

The earliest single-mode R-T experiments were carried out by Lewis (1950), using fluids of different densities in a vertical tube accelerated by air pressure. Emmons *et al.* (1960) generated a pressure gradient by accelerating a tank containing methanol and air along guide rails. Read (1984) was the first to perform experiments that investigated multimode R-T driven mixing. He used solid-fuel rockets to generate accelerations up to $76g$, although the experiment allowed only a few milliseconds of data collection time. Early work on buoyancy-driven flows include the experiments of Jevons (1857) who studied the formation of cirrus cloud formation through a thermal inversion of a stable interface. Dimonte & Schneider (1996) used a set-up similar to Read (1984), but with the acceleration provided by linear electric motors. Both experiments were capable of handling large density differences. Other methods of obtaining an unstably stratified interface include quickly overturning a narrow box filled with the light fluid on top of the heavy (Andrews 1986; Andrews & Spalding 1990), and withdrawing a plate that initially separates the two fluids (Linden *et al.* 1994; Dalziel, Linden & Youngs 1999). All these experiments have short data collection times, and require a large number of repeat runs which has limited the extent of statistical data collection.

Recent advances in modelling of buoyancy-driven turbulence include the spectral transport model (Besnard *et al.* 1990, 1992; Steinkamp 1995; Steinkamp, Clark & Harlow 1995; Wilson, Andrews & Harlow 1999), the two-fluid models (Andrews 1986; Youngs 1989), and the Reynolds stress/Bousinesq models (Snider & Andrews 1996). All of these advanced models for R-T mixing require detailed measures of turbulent quantities such as $\overline{\rho'^2}$, $\overline{u'^2}$, $\overline{v'^2}$, $\overline{u'v'}$, and $\overline{u'v'v'}$ to validate closure models. Although these quantities may be computed from direct numerical simulations (DNS), such calculations are limited to relatively low Reynolds numbers; thus, there is a continuing need to obtain these quantities experimentally. A recent high-resolution simulation by Cook & Dimotakis (2001) was performed at Taylor Reynolds numbers of up to 100, the threshold for mixing transition (Dimotakis 2000). Such a simulation constitutes one realization of the spatially evolving mixing layer in the current experiment and is typical for the current state-of-the-art of DNS of R-T mixing. Thus, the R-T mix represents a leading grand challenge problem in the DNS of turbulent flows, placing stringent requirements on resolution in time and space, and desired ensemble averages. We also note the prevalence of large-eddy simulation (LES) techniques in the study of R-T flows, especially at high Reynolds numbers. The monotone integrated large-eddy simulation technique (MILES) has been shown to be particularly attractive in the study of flows with discontinuities such as R-T (Youngs 2003).

To predict the turbulent mixing that occurs within the self-similar region, it is important to understand the mechanisms and structure of the turbulent flow field. In this paper, we do this through studying measurements of turbulent velocity and density fields. Andrews and collaborators (Snider & Andrews 1994; Wilson *et al.* 1999; Wilson & Andrews 2002) have developed a statistically steady low-Atwood-number Rayleigh–Taylor mixing experiment based on the concurrent flow off the end of a splitter plate of cold (ρ_c) water over hot (ρ_h). The experiment permits extended data collection times (10 min or longer), with collection of statistically convergent data, and does not have long time transients. In the present work, we employed particle image velocimetry (PIV) to investigate R-T mixing. We note that Prestridge *et al.* (2000) used PIV and flow-visualization techniques to observe the instantaneous two-dimensional velocity and density fields in their Richtmeyer–Meshkov experiments. Dalziel (1993) used particle tracking velocimetry to investigate low-Atwood-number mixing in his

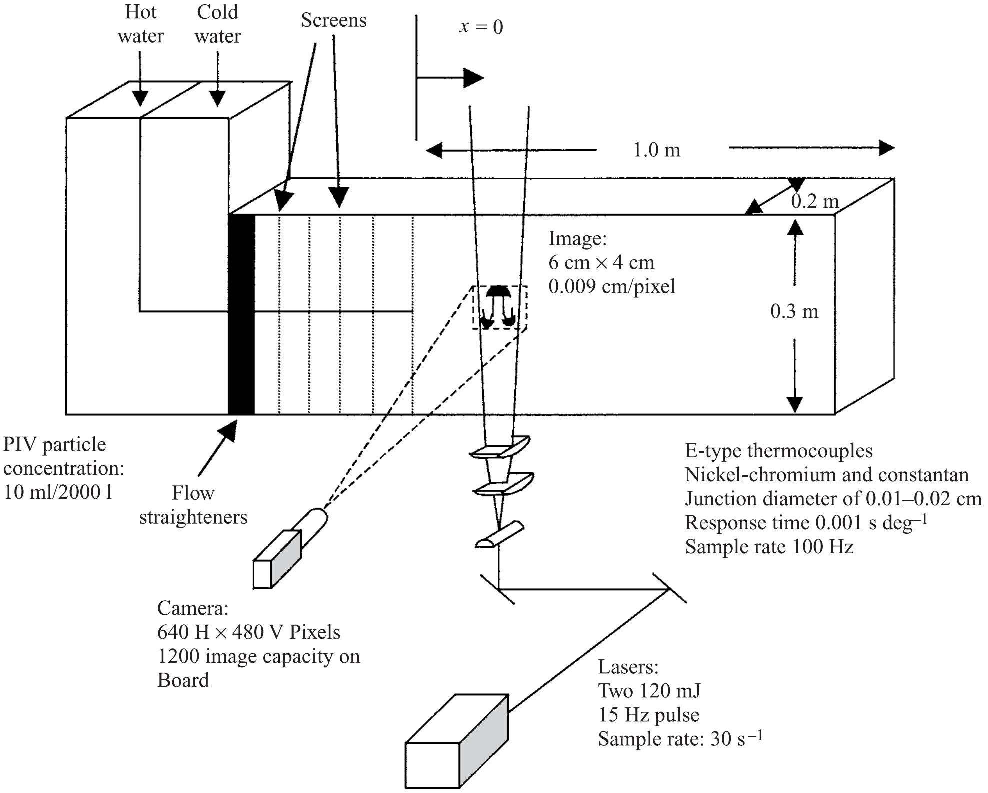

FIGURE 3. Schematic of experimental set-up.

tank and barrier experiments. In this study, turbulence quantities and their spectra were determined from detailed two-dimensional slices of three-dimensional turbulent velocity fields obtained using PIV (for a review of PIV techniques, see Adrian 1991), and from high-resolution single-point thermocouple measurements. Independently, Lawrence, Browand & Redekopp (1991) used a related experimental set-up in their study of compound mixing due to shear and a stable density stratification. Another version of the experiment can be seen at the end of the film by Stewart (1968).

2. Experiment

The experimental set-up is shown in figure 3. The channel consisted of upper and lower entry plenums separated by a splitter plate. The cold-water channel was fed from a 500 gallon tank, and a second lagged 500 gallon tank of warm water fed into the lower channel. The cold and warm water streams entered the channel at a mean velocity of $\sim 4.4\,\mathrm{cm\,s^{-1}}$. The density difference was achieved through a temperature difference of 5 °C–10 °C in the water. Temperature data were converted to density through the following equation of state (Kukulka 1981):

$$\rho = (999.8396 + 18.2249\Theta - 0.007922\Theta^2 - 55.448 \times 10^{-6}\Theta^3 + 149.756 \times 10^{-9}\Theta^4 - 393.295 \times 10^{-12}\Theta^5)/(1 + 18.159 \times 10^{-3}\Theta), \tag{4}$$

where Θ is in centigrade degrees, and ρ is in $\mathrm{kg\,m^{-3}}$. The above expression is nearly linear at temperatures in the range of 15 °C–25 °C for the present experiment. Both tanks contained sump pumps to ensure a uniform temperature was maintained in the tanks throughout the experiment. Thus, cold (heavier) water entered through the top plenum, while warm (lighter) water entered through the lower plenum, and the two streams formed an unstable Rayleigh–Taylor mix as they left the edge of the splitter plate. The resulting flow was statistically steady, allowing for long data collection times, albeit at small Atwood numbers $A_t < 10^{-3}$. No shear between the two fluid streams was employed in the present work. Nigrosine dye was injected at the splitter plate, and the flow velocities were adjusted until the dye was convected downstream without undergoing any distortion due to shear. From mean velocity profiles across the mix at late-time, the amount of shear was determined to be $\sim 1\%$ of the mean convective velocity. The flow channel was 241 cm long (including the inlet and exit plenums), 31 cm deep, and 15 cm wide. At this width, the front and back walls of the channel did not have any effect on the development of the mix in the central region (Snider & Andrews 1994). The test section was 100 cm long. The splitter plate was 0.32 cm thick, with a 2.5° knife-edge. Calibrated rotameters were used to regulate the mean flow rate. Screens and flow straighteners in each of the plenums minimized free-stream turbulence (Snider & Andrews 1994) and suppressed the growth of boundary layers on the walls. As figure 2 shows, and was discussed in the last section, any velocity defect from the boundary layers is smoothed out rapidly (by $x \sim 2$ cm) owing to the buoyancy-driven vertical transport of momentum and to diffusion. A fine mesh (35 mesh/in.) at the end of the splitter plate absorbed some of the momentum deficit introduced by the knife-edge.

2.1. *PIV system*

The PIV system consisted of two Nd-YAG lasers that fire alternately, each at a rate of 15 Hz, giving a net sampling rate of 30 Hz. The pulse duration of the lasers was 5 ns, ensuring that the images represented the instantaneous positions of the particles. The laser beam was passed through an array of cylindrical lenses to produce a laser sheet of thickness less than 1 mm. Neutrally buoyant, hollow silvered spheres of diameter 10 μm were used to seed the flow. Seed particle concentrations were varied from 3 ml to 6 ml per 500 gallons of the cold and hot water, and were well stirred into the water by the sump pumps. A KODAK Megaplus digital camera, triggered synchronously with the lasers, was used to record the images with arrays of 640 × 480 pixels. Typically, 1200 images were collected to obtain convergent statistics (Ramaprabhu & Andrews 2003). A *labview* based system was used to control triggering of the lasers and data collection.

The displacement of a particle in two successive images gives the velocity vector at that point. Our requirements for PIV were standard, and so we used the readily available MATPIV program, a cross-correlation-based software package (Grue *et al.* 2000). The cross-correlation function $R(x, y)$ was computed from the two image fields, I_1 and I_2 as

$$R(x, y) = \sum_{i=-M/2}^{M/2} \sum_{j=-N/2}^{N/2} I_1(i, j) I_2(i + x, j + y), \tag{5}$$

where $M = N = 2^n - 1$; $n = 3, 4, 5 \ldots$. The mean intensities were subtracted from I_1 and I_2 and the resulting value of $R(x, y)$ was normalized by the correlation coefficient. The location of the correlation peak with respect to the centre of the interrogation window gives the local displacement vector. The vector field is smoothed by a signal-to-noise ratio filter and a global histogram filter. Vectors with a signal-to-noise ratio less than 1.1 or lying outside two standard deviations of the neighbouring vectors were replaced by interpolated values. The PIV software yields 1199 vector fields from the 1200 greyscale images. First-, second-, and third-order statistics were computed from the vector fields. One concern is that local density variations can influence the refractive index, resulting in an apparent displacement of the particle position along the line of sight. However, for the low values of density differences used in this experiment, and the short beam traverse distances along the line of sight, this effect was explored and found negligible (Ramaprabhu & Andrews 2003). Following the method of Adrian (1997), we determined the error in our velocity measurements to be $\sim \pm 0.05\,\mathrm{cm\,s^{-1}}$ based on the uncertainty associated with the location of a particle.

2.2. *Thermocouple system*

The temperature diagnostics consisted of a vertical rake of thermocouples that were positioned at different downstream locations in the channel. The thermocouple probes were E-type (nickel-chromium and constantan) and welded at the tip to form a bimetallic junction. The thermal response of the E-type thermocouple was $\sim 0.001\,\mathrm{s\,deg^{-1}}$ (Wilson & Andrews 2002), while the accuracy was ± 0.1 deg. A 16-bit data acquisition board collected data from the thermocouples at a maximum sampling rate of 100 000 Hz. To remove some of the noise, local averages of over 1000 samples were performed, resulting in a net sample rate of 100 Hz. The welded thermocouple probe tip was approximately 0.01 cm in diameter. At a downstream distance of 30 cm from the splitter plate, a local mixing Reynolds number may be computed by balancing the potential energy released against the turbulent kinetic energy of the flow to obtain (Snider & Andrews 1994)

$$Re_x^a = \sqrt{\frac{gA_t}{6}}\frac{(2h_x)^{3/2}}{\nu}, \tag{6}$$

where h_x is the mix width (taken to be the distance between points where the mean density is 5% and 95% of the cold or hot fluid) at a downstream distance x. At this location, the Kolmogorov turbulent scale (η_k) is given by

$$\eta_k = h_x Re_x^{a^{-3/4}}. \tag{7}$$

The corresponding Batchelor scale (η_B), which is relevant for scalar (thermal/density) fluctuations is

$$\eta_B = \eta_k\, Pr^{-1/2}, \tag{8}$$

where Pr is the Prandtl number ($Pr \sim 7$ for water at 20 °C). At $x = 30\,\mathrm{cm}$, (8) gives $\eta_B = 0.02\,\mathrm{cm}$, which suggests that the Nyquist resolution criterion is satisfied at the current sampling rates. However, for $x > 30\,\mathrm{cm}$, this criterion is not met, and the smallest scales of turbulent motion may not be fully resolved. The data collection time was $\sim 160\,\mathrm{s}$, which was chosen to allow more than 80 of the largest-scale structures to be recorded (the turnover time of the large-scale structures is given by $\mathscr{T} = 2h_x/U \sim 2\,\mathrm{s}$, where U is the mean convective velocity of the flow). The long data collection times and the high sampling rate resulted in capturing almost four decades of frequencies. The configuration and details of the thermocouple system are further described in Wilson & Andrews (2002), with a detailed consideration of the Batchelor scale.

In (6), the Reynolds number was defined assuming that all the initial potential energy in h_x associated with the unstable density interface was converted completely to kinetic energy. In a buoyancy-driven mix with no shear, the mean convective velocity does not contribute to the dynamics of the buoyant mix. As a result, the definition of a Reynolds number often becomes a matter of preference depending on

Equation	Definition	Re
(6)	$\sqrt{\frac{gA_t}{6}}\frac{(2h_x)^{3/2}}{\nu}$	1450
(9)	$\frac{h_x\dot{h}_x}{\nu}$	1000
(10)	$\frac{h_x v_\infty}{\nu}$	1250
(11)	$v'\lambda/\nu$	60

TABLE 1. Reynolds number definitions for R-T flow.

the choice of a suitable velocity scale. Some commonly used definitions are reviewed here. The self-similar nature of this flow may be incorporated into a Reynolds number definition by using the mix width as the length scale, and its time derivative as the corresponding velocity scale (Cook & Dimotakis 2001):

$$Re_x^b = \frac{h_x\dot{h}_x}{\nu}. \tag{9}$$

An alternative definition uses the terminal velocity introduced earlier as the velocity scale, resulting in a form close to (6):

$$Re_x^c = \frac{v_\infty 2h_x}{\nu} = \frac{2h_x}{\nu}\,0.7\sqrt{A_t g h_x/2}. \tag{10}$$

Implicit in (9) is the use of a root mean square (r.m.s) velocity scale $v' \sim \dot{h}_x$, whereas (10) uses the terminal velocity of the bubbles in this flow. Finally, at the microscales, a Taylor Reynolds number may be defined based on the Taylor length scale λ and the r.m.s. velocity scale:

$$Re_\lambda = \frac{\lambda v'}{\nu}. \tag{11}$$

The Taylor Reynolds number is a universal measure of the state of turbulence since it is defined independent of the large-scale features of the flow. For instance, it has been argued that a Taylor Reynolds number of 100 is required to cross the mixing transition threshold for all turbulent flows (Dimotakis 2000). The Reynolds numbers computed from the above definitions are given in table 1 for $x = 35$ cm. All the definitions based on large-scale features of the flow have similar values of the Reynolds numbers, indicating that these different velocity and length-scale definitions are equivalent.

2.3. *PIV-S*

To measure velocity and density fields simultaneously, a whole-field non-intrusive technique called PIV-scalar or PIV-S (Ramaprabhu & Andrews 2003) was used. PIV-S involves seeding the two fluids with different concentrations of seed particles (figure 12 shows an example photograph), and was shown to work well (Ramaprabhu & Andrews 2003) in the present flow where the velocity jump between fluids is negligible, and the density difference is small. Typically, the cold fluid was seeded with twice as many particles as the hot fluid. The local average of the reflected light intensity can

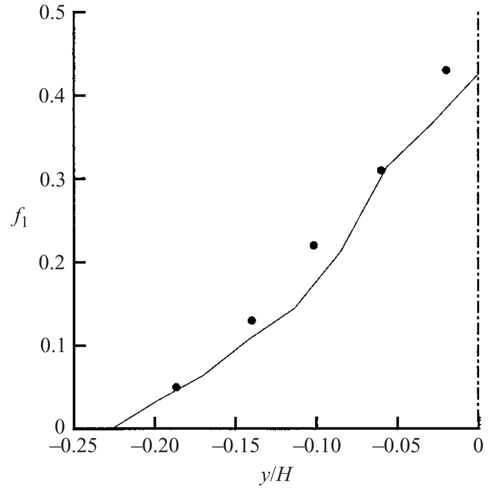

FIGURE 4. Volume fraction profiles from PIV-S (solid line), and thermocouple (circles) at $T \sim 1.21$.

be related to the density at that point. Thus,

$$\rho(x_x, y_c) \propto \frac{1}{A}\int I(x, y)\,\mathrm{d}A \propto \sum_{j,k=1}^{N} I(x_j, y_k). \qquad (12)$$

The constant of proportionality in (12) need not be determined in the implementation of this technique, thus removing the necessity for calibration runs. First-order density statistics from this method agree well with those obtained from thermocouple measurements at the same locations. Figure 4 is a comparison of mean volume fraction (a non-dimensional density defined in § 3) profiles from both methods at $x \sim 35$ cm. Only the lower half of the mix-width is shown, and the y-coordinate is normalized by the depth of the channel H. Section 3 of this paper also describes good agreement for the second-order statistics at the centreline of the mix. Away from the centreline, however, the high Schmidt number of the seed particles compared with the Prandtl number leads to lower estimates of the amount of mixing. In particular, the molecular mix, a mix parameter computed from this method and described below, approaches a two-fluid (immiscible) limit near the edges of the mix. Also, the spatial resolution of PIV-S is poor owing to the local averaging process. Nevertheless, there is valuable information here, because simultaneous measurements of mean profiles of density and r.m.s. velocities from PIV-S allow calculation of a global energy budget and, consequently, the energy dissipation in this flow (§ 5).

3. Results and discussion

High-resolution ($\Delta x = \Delta y = 0.03$ cm) velocity data were collected at a sampling rate of 30 Hz at 2 cm and 35 cm downstream from the splitter plate. Thus, the smallest length scales captured with this technique are ~ 0.06 cm. The data collected just off the splitter plate, at 2 cm, represent the initial conditions of the flow. The fine-mesh screen at the edge of the splitter plate creates a ‘grid-type’ turbulence, with a spectrum of velocity perturbations in its wake. At 35 cm downstream, the hot and cold fluids are well mixed and the flow has reached an observed self-similar state. The data presented

	X-location (cm)	T-location	Y-location (cm)	Resolution
Thermocouple	1.0	0.03	0	$\Delta t = 0.01$ s
	2.0	0.07	0	
	10.0	0.34	0	
	20.0	0.70	0	
	30.0	1.00	0	
	40.0	1.39	0	
	50.0	1.74	0	
	60.0	2.08	0	
PIV (low resolution)	0–8.0	0–0.305	−3.0–3.0	$\Delta t = 0.066$ s
	8.0–16.0	0.305–0.610	−3.0–3.0	$\Delta x = \Delta y = 0.2$ cm
	16.0–24.0	0.610–0.916	−6.0–6.0	
	24.0–32.0	0.916–1.221	−9.0–9.0	
	32.0–40.0	1.221–1.527	−9.0–9.0	
	40.0–48.0	1.527–1.832	−9.0–9.0	
	48.0–56.0	1.832–2.137	−9.0–9.0	
PIV (high resolution) PIV-S	2.0	0.07	0.0	$\Delta t = 0.033$ s
	35.0	1.21	0.0	$\Delta x = \Delta y = 0.03$ cm

TABLE 2. Thermocouple and PIV/PIV-S experiments.

here describe the more fully developed R-T mix. In addition, lower resolution ($\Delta x = \Delta y = 0.2$ cm) velocity data were collected at x-locations ranging from 0 to 56 cm from a series of experiments each with a window size of 8 cm × 6 cm (table 2). The data-sampling rate used in these lower resolution experiments was 15 Hz, and these velocity fields were primarily used for computing the statistics at these locations. The small velocity scales that are not resolved by this set of experiments contribute little to the statistics here because of their small amount of energy.

Following Dalziel *et al.* (1999), we define a dimensionless time

$$T = t\left(\frac{A_t g}{H}\right)^{1/2} = \frac{x}{U}\left(\frac{A_t g}{H}\right)^{1/2}. \tag{13}$$

Here, the downstream distance x is converted to time t, using the Taylor hypothesis, $t = x/U$. The definition of T incorporates the self-similar nature of the flow (here, g is the acceleration due to gravity, x is the downstream distance, U is the mean convective velocity, and H the depth of the channel). In self-similar units, the two locations $x = 2$ cm and 35 cm (where the high-resolution data were collected) correspond to $T = 0.07$ and 1.21, respectively. The early- and late-time PLIF images from figure 2, were taken at $T \sim 0$–0.305 and $T \sim 1.22$–1.52, respectively. The low-resolution PIV experiments were performed at $0 < T < 2.1$. The mix width plots of Dalziel *et al.* (1999) show a quadratic growth for $T > 1$, indicating the onset of self-similarity. Temperature data were collected by thermocouples along the centreline of the mix at 8 downstream locations (the location of the centreline was determined by a false positioning method described in Ramaprabhu & Andrews 2003). These locations correspond to $0.03 < T < 2.08$. In all of the experiments presented here, care was taken to eliminate shear between the two fluid streams. Table 2 is a summary of all the experiments reported in this paper.

The range of temperature fluctuations and the extent of mixing in a Rayleigh–Taylor flow are characterized by the following parameters:

$$\left.\begin{aligned}
&f_1 = \lim_{T\to\infty}\frac{1}{T}\int_0^T \frac{\rho-\rho_2}{\rho_1-\rho_2}\,\mathrm{d}t = \lim_{T\to\infty}\frac{1}{T}\int_0^T \frac{\rho-\rho_h}{\rho_c-\rho_h}\,\mathrm{d}t,\\
&f_2 = 1-f_1,\\
&B_0 = \lim_{T\to\infty}\frac{1}{T}\int_0^T (\rho-\overline{\rho})^2\,\mathrm{d}t/\Delta\rho^2,\\
&B_2 = f_1 f_2 = f_1(1-f_1),\\
&\theta = 1-\frac{B_0}{B_2},
\end{aligned}\right\} \tag{14}$$

where f_i is the fraction by volume of the ith fluid (with $f_1 = f_{cold}$ and $f_2 = f_{hot}$), and ρ is obtained from (4) using thermocouple measurements, or from (12) from the PIV-S measurements. Then, B_0 is the intensity of turbulent density fluctuations and includes the effect of mixing due to molecular diffusion; B_2 is the corresponding conditioned measure that would result if the two fluids were immiscible and does not account for molecular mixing; and the parameter θ (Dankwerts 1952) quantifies the degree of mixing ($\theta = 0 \rightarrow$ no mixing, and $\theta = 1 \rightarrow$ completely molecularly mixed fluids). As explained in more detail later, B_2 may also be interpreted as an intermittency factor based on the density of the fluids.

The molecular mix θ affects the overall growth rate of the mix in the following way. Consider the definitions of B_0 and B_2 as the non-dimensional turbulent density fluctuations in the presence and absence of molecular diffusion, respectively. Then,

$$B_0 = \overline{\rho_0'^2}/\Delta\rho^2, \quad B_2 = f_1 f_2 = \overline{\rho_2'^2}/\Delta\rho^2, \tag{15}$$

where the $\overline{\rho_0'^2}$ and $\overline{\rho_2'^2}$ refer to the turbulent density fluctuations for the miscible and two-fluid cases, respectively, and $\Delta\rho = \rho_1 - \rho_2$. Equation (1) for the growth rate of the mix may be rewritten using the modified driving term $2\sqrt{\overline{\rho_0'^2}}$

$$h = 2gt^2\alpha\sqrt{\overline{\rho_0'^2}}/(\rho_1+\rho_2). \tag{16}$$

This is a more natural choice for molecularly mixed fluids, since the density difference available to drive the flow $\Delta\rho = \rho_1 - \rho_2$ is reduced in the presence of diffusion. For a two-fluid case at the centreline where $f_1 = f_2 = 0.5$, then

$$\overline{\rho_0'^2} = \overline{\rho_2'^2} = f_1 f_2 \Delta\rho^2 = (\rho_1-\rho_2)^2/4, \tag{17}$$

so that (16) reduces to (1).

For miscible fluids, we have

$$\frac{\overline{\rho_0'^2}}{\overline{\rho_2'^2}} = \frac{B_0}{B_2} = 1-\theta, \tag{18}$$

reducing (16) to

$$h = \tilde{\alpha} A_t g t^2, \tag{19}$$

where $\tilde{\alpha} = \alpha\sqrt{1-\theta}$. At the centreline of the mix, measurements of θ have been found to vary from 0.7 to 0.8 (Wilson & Andrews 2002), and remain reasonably constant across the mix (see below). Assuming an intermediate value of $\theta = 0.75$, the presence

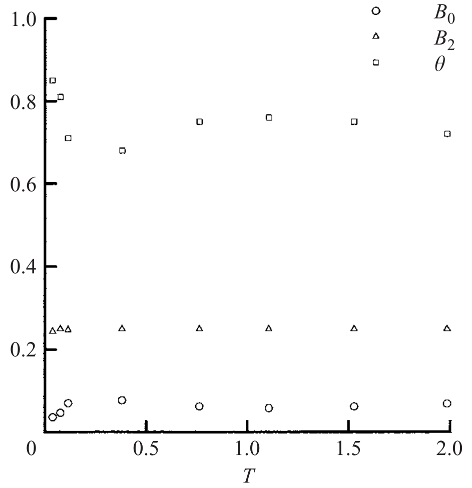

FIGURE 5. Time evolution of scalar turbulence intensity and mix parameters measured at the centreline.

of molecular diffusion serves to reduce the growth rate of the mix by a factor of 0.5. The front tracking calculations of Glimm *et al.* (2001) suggest a two-fluid value for α of 0.07, giving a net growth constant $\tilde{\alpha} = 0.5\alpha = 0.035$. This is consistent with the value reported by most numerical simulations that have molecular diffusion in them.

The centreline time-evolution of the mix-parameters defined above and determined from the thermocouple measurements, are shown in figure 5. Close to the splitter plate ($T \sim 0.034$), the mixing layer is diffuse and, as a result, θ values are high in this region (and corresponding B_0 values are low). As the mix develops farther downstream, the fluctuation levels increase with the onset of the instability, resulting in a slight drop in the value of θ. This corresponds to the stretching of the initial diffuse layer, followed by rolling up into mushroom-shaped structures. This is also seen in the p.d.f.s of density values (figure 6), which switch from an initial distribution with a single peak ($T = 0.034$) suggesting a diffuse region, to a distinctly bimodal distribution at later times ($T = 0.347$), indicating fluctuating density fields. Eventually ($T = 1.008$), turbulent diffusion serves to smooth out some of these fluctuations, and the histogram regains a dominant peak corresponding to $(\rho - \rho_2)/(\rho_1 + \rho_2) = 0.5$ at the centre of the mix. As expected, the two-fluid parameter B_2 remains relatively constant at a value of 0.25. This further confirms that these measurements were indeed at the centreline of the mix, since at the centre $f_1 = f_2 = 0.5$ and $B_2 = 0.25$ according to (14). It is noteworthy that all the parameters change little in the developing self-similar regime of the mix ($T > 1$).

The mix parameter θ may also be measured from the two-dimensional density fields obtained from PIV-S. The results are compared with thermocouple measurements across the mix at $x = 35$ cm or $T = 1.21$ (figure 7). There is good agreement between the two measurements at the centreline because it is a well-mixed region containing a preponderance of small-scale velocities, as described later. Away from the centre, θ_{PIVS} approaches a two-fluid value of zero, whereas the thermocouple measurement indicates θ is reasonably constant across the mix. The lower diffusivity of seed particles compared with thermal diffusivity causes the underestimation of θ that is seen in these PIV-S measurements. It is interesting to note that R-T experiments, where salt was used to create the density difference (Dalziel *et al.* 1999), also give similar θ values

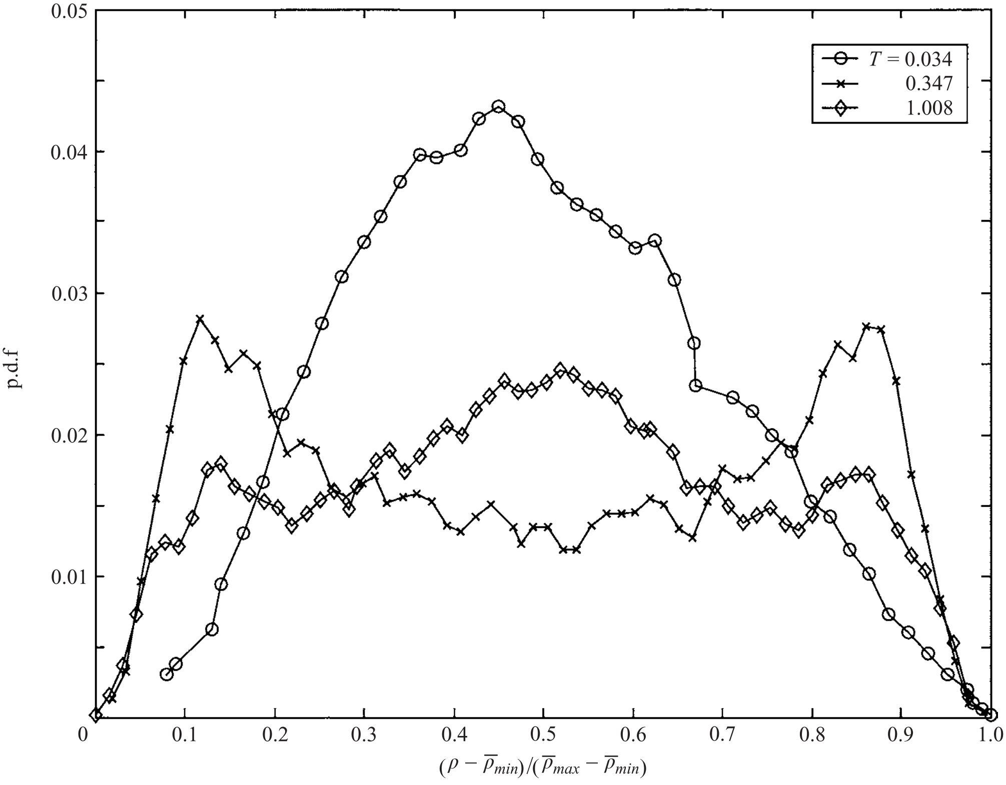

FIGURE 6. Probability density functions of centreline non-dimensional density at three different times.

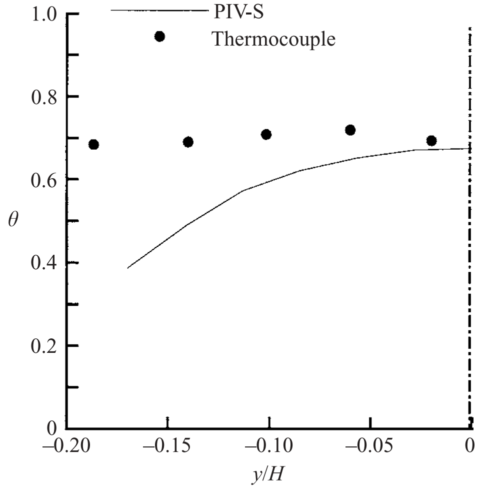

FIGURE 7. Profiles of θ from PIV-S and thermocouple at $T = 1.21$.

at the centreline in spite of the much lower mass diffusivity of salt compared with the thermal diffusivity. So, near the centreline where mixing is highest, the difference between an estimated particle Schmidt number (> 600), and the Prandtl number (~ 7) does not seem to play a role. This is because the centre of the mix region has

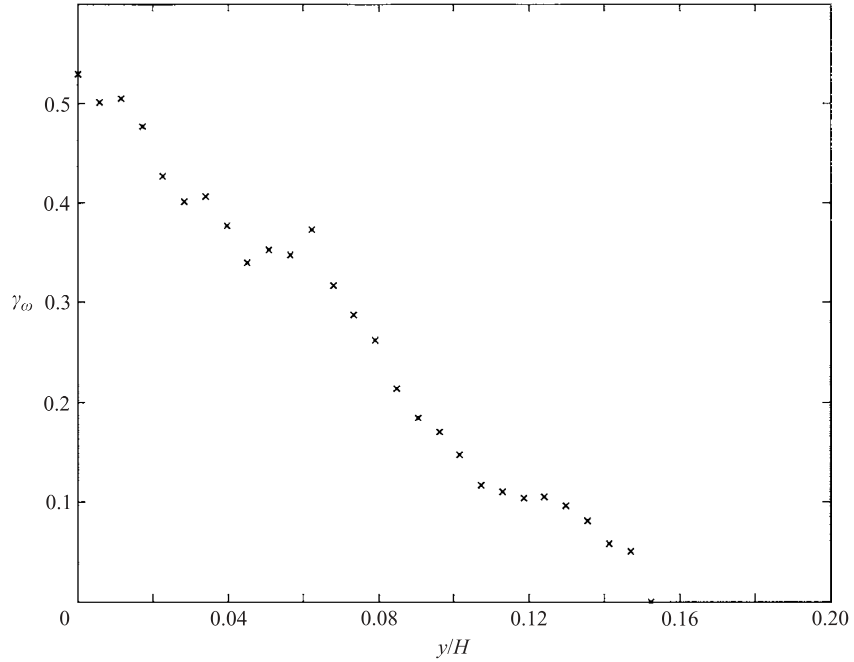

FIGURE 8. Intermittency factor γ (based on a vorticity threshold) across the mix at $T = 1.21$.

more interfacial area than the edge, resulting in greater molecular diffusion and thus molecular mixing. From a spatial convergence test (Ramaprabhu & Andrews 2003), the volume fraction values were found to be reasonably constant for window sizes between 16 and 32 pixels. For windows smaller than 16 pixels, the volume fraction was found to approach two-fluid values owing to lack of sufficient samples for averaging. Similarly, the value of θ is reasonably constant for window sizes between 16 and 32 pixels, and again approaches a two-fluid value for windows smaller than 16 pixels.

We attempt to quantify this by defining an appropriate intermittency factor γ. A common definition of intermittency focuses on the vorticity in the fluid, γ_ω, i.e. rotational fluid is marked as turbulent fluid, and irrotational fluid is marked as quiescent. An intermittency function, I, based upon vorticity is defined as (Pope 2000)

$$I(y,t) = \mathscr{H}(|\omega(y,t)| - \omega_{threshold}), \tag{20}$$

where ω is the out-of-plane component of the local vorticity field, $\omega_{threshold}$ is a small positive threshold, and $\mathscr{H}$ is the Heaviside function. Thus, I is 1 for $|\omega| > \omega_{threshold}$ and zero otherwise. The intermittency factor is then given by

$$\gamma_\omega(y) = \langle I(y,t)\rangle, \tag{21}$$

where $\langle\cdot\rangle$ indicates time-averaging. In the present experiment, the cross-stream (vertical) profile of γ_ω is shown in figure 8 for $T = 1.21$ ($\omega_{threshold}$ was chosen so that $\omega^2_{threshold}/\langle\omega\rangle^2$ was $\sim 5\%$). Unlike shear layers and wakes, where γ_ω can reach a maximum value of 1 at the centreline (LaRue & Libby 1976), the intermittency factor reaches a peak value of 0.5 in our buoyancy-driven mix. This is due to significant cross-stream transport of rotational and irrotational fluid, thus decreasing the value at the centreline. However, this picture is incomplete, as we will show in the following. For our purposes, we are interested in identifying the interface between the heavy and

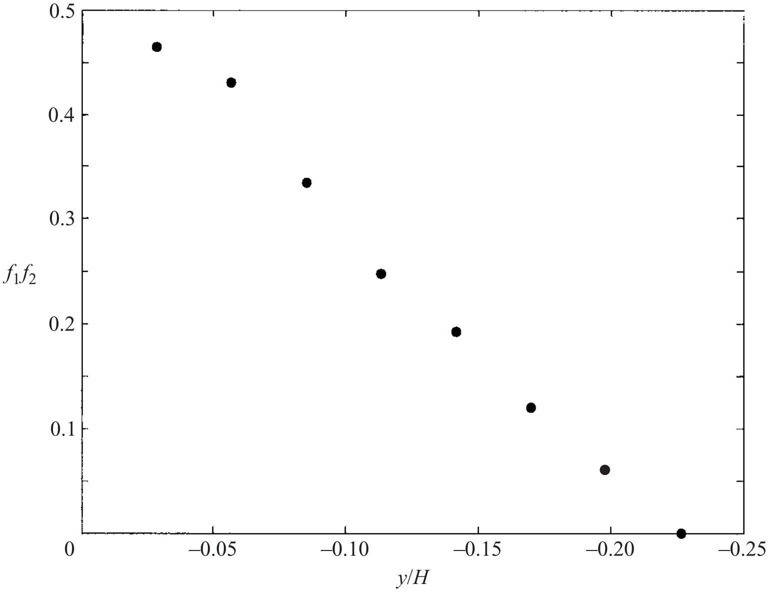

FIGURE 9. Intermittency factor (based on the two-fluid parameter B_2) across the mix at $T = 1.21$.

light fluids. Therefore, a more natural definition for the present buoyant mixing is an intermittency factor (or a density intermittency factor) based on the volume fraction.

We take $f_{threshold} = 0.5$ as the threshold for defining a density intermittency factor. Then, using the Heaviside function and instantaneous volume fractions $f_1' = (\rho - \rho_2)/(\rho_1 - \rho_2)$, $f_2' = 1 - f_1'$, we may define

$$N^+(y,t) = \mathscr{H}(f_1'(y,t) - f_{threshold}),$$
$$N^-(y,t) = \mathscr{H}(f_{threshold} - f_2'(y,t)).$$

Hence, $\langle N^+(y,t)\rangle$ and $\langle N^-(y,t)\rangle$ denote the probability of finding fluid 1 and 2, respectively, at y; thus, $\langle N^+(y,t)\rangle \cong f_1$, and $\langle N^-(y,t)\rangle \cong f_2$ by definition of volume fraction. Any definition of density intermittency will have to include the volume fraction of the fluid, which can be interpreted as a conditional measure of the density of the fluid and be symmetric about the centreline of the mix. This may be accomplished by defining a density intermittency factor as

$$\gamma_\rho = \tfrac{1}{2}(1 - (\langle N^+(y,t)\rangle - \langle N^-(y,t)\rangle)^2) = \tfrac{1}{2}((f_1 + f_2)^2 - (f_1 - f_2)^2), \tag{22}$$

using $f_1 + f_2 = 1$. In the above, the $f_{threshold}$ term is eliminated when the Heaviside operation is performed. This definition ensures that γ_ρ reaches a peak value of 0.5 at the centreline where $f_1 = f_2 = 0.5$ and goes to zero at the edges where $f_1 = 1 - f_2 = 0$ and vice versa. After some algebraic manipulation, (22) simplifies to

$$\gamma_\rho = 2f_1f_2 = 2B_2. \tag{23}$$

Thus, a γ_ρ value of zero implies the presence of a single fluid, and a value of 0.5 indicates that both fluids are present with equal probability (i.e. a large amount of density intermittency). Figure 9 plots γ_ρ as a function of y/H at $T = 1.21$ and shows a peak value of 0.5 at the centreline. This indicates the presence of a large amount of density intermittency as well as associated interfacial area at the centreline with a value approaching the single-fluid limit at the edge of the mix. Thus, the structures

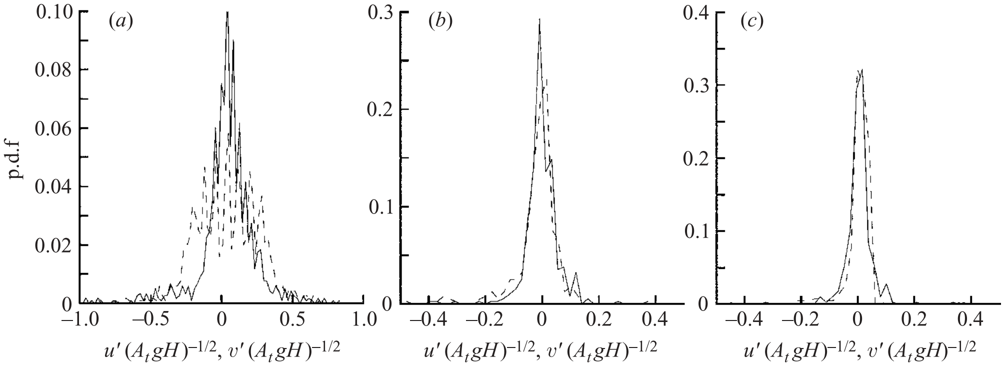

FIGURE 10. Probability density functions of vertical and horizontal velocities at three locations across the mix. (*a*) $v'/v'_{max} = 1$, (*b*) $v'/v'_{max} = 0.5$, (*c*) $v'/v'_{max} = 0.2$ corresponding to $y/H = 0, 0.13$ and 0.2 respectively ($T = 1.21$). ——, u'; – – –, v'.

at the centreline are much more contorted, with greater interfacial area resulting in molecular diffusion across the interface, as shown in figure 2(*b*).

These observations are also supported by velocity p.d.f.s at $T = 1.14$ for three locations across the mix: at points where $v'/v'_{max} = 1$, 0.5, and 0.2 corresponding to $y/H = 0, 0.13$ and 0.2, respectively (figures 10(*a*), 10(*b*) and 10(*c*), respectively) with v'_{max} available from figure 16(*b*). The resolution in all three figures is the same, i.e. the number of intervals across the dynamic range of the velocities is constant. At the centre of the mix, where $v'/v'_{max} = 1$, the vertical velocity distribution is flatter than the horizontal velocity components and covers a wider range of scales; thus, the likelihood of finding large velocities is roughly the same as that of finding small velocities. This implies that there is a greater hierarchy of scales at the centre of the mix, resulting in a greater interfacial area and hence enhanced mixing. Approaching the edge of the mix with $v'/v'_{max} = 0.5$ and then 0.2, for both the horizontal and vertical components, small velocities become more likely than large ones. In addition, the vertical velocity p.d.f.s become more skewed and less Gaussian near the edge for reasons explained by considering the skewness below.

The third and fourth moments of the velocity field represent the skewness and flatness (kurtosis) of the velocity probability density functions. These functions are conventionally normalized by the velocity r.m.s.:

$$S_u = \frac{\langle u'^3 \rangle}{\langle u'^2 \rangle^{3/2}}, \quad S_v = \frac{\langle v'^3 \rangle}{\langle v'^2 \rangle^{3/2}}, \quad K_u = \frac{\langle u'^4 \rangle}{\langle u'^2 \rangle^2}, \quad K_v = \frac{\langle v'^4 \rangle}{\langle v'^2 \rangle^2}, \tag{24}$$

where $\langle u'^2 \rangle$ and $\langle v'^2 \rangle$ profiles are given in figures 16(*a*) and 16(*b*), respectively. Cross-stream profiles of the skewness and kurtosis of the horizontal and vertical velocity distributions are shown in figures 11(*a*) and 11(*b*), respectively. S_u is close to zero across the mix, since the horizontal velocity field is symmetric about the vertical. However, S_v, is zero at the centreline and antisymmetric about it. Alternatively, the predominant velocity determines the sign of skewness, because of the third power. It may be noted that $S_v > 0$, for $y > 0$, as fluid is predominantly rising (the upper edge of the mix), whereas $S_v < 0$ for $y < 0$ as fluid is predominantly falling (lower edge of the mix). Neglecting the horizontal velocities, which cancel out due to symmetry, mass conservation for the mix considered as a two-phase fluid gives $f_1 v_1 + f_2 v_2 = 0$, where f_1, f_2 and v_1, v_2 are the volume-fraction and the vertical velocity components of the heavy and light fluids, respectively. At the centreline, $f_1 = f_2 = 0.5$ and $v_1 = - v_2$,

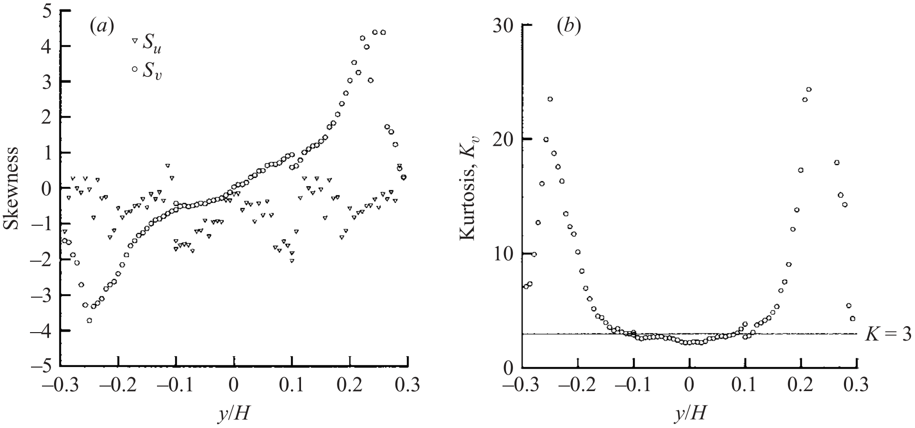

FIGURE 11. (*a*) Skewness and (*b*) kurtosis profiles across the mix at $T = 1.21$.

resulting in a symmetric p.d.f. and $S_v = 0$. At the edge, $f_1 \rightarrow 1$ (and $f_2 \rightarrow 0$) v_1 is a small negative velocity while v_2 is a large positive velocity. Conversely, as $f_1 \rightarrow 0$, v_1 is a large negative velocity and v_2 has a small positive value. Thus, the vertical velocity skewness profile is zero at the centreline, with positive values for $y > 0$ and negative values for $y < 0$. (Beyond the edge of the mix, the skewness drops to zero owing to the presence of random noise.)

The fourth moment of velocity, the kurtosis, is shown in figure 11(*b*). For a Gaussian p.d.f., the skewness is zero and the kurtosis approaches a value of three. In the present case, the vertical component K_v approaches the Gaussian value ($K = 3$) at the centreline and is highly non-Gaussian at the edges. This is in agreement with the skewness data, which also show Gaussian behaviour at the centre, and a non-Gaussian trend at the edges. The symmetric profile of K_v arises from taking the fourth power of the velocity fluctuations. The *u*-component has considerable jitter across the mix, which are amplified when raised to the fourth power and is not shown in figure 11(*b*).

We conclude that the presence of both fluids with equal probability, associated with a high intermittency factor, and the hierarchy of scales, all contribute to the enhanced mixing measured at the centreline. The next section is divided into three subsections based on the nature of the velocity data presented, namely qualitative aspects, statistics and spectral data.

3.1. *Qualitative aspects*

Figure 12 shows a pair of successive PIV-S images (separated by a time interval of 0.033 s), in which the heavy fluid is seeded with a higher concentration of particles than the lighter fluid. The difference in particle concentrations delineates the structures in the flow. The images are 640 × 480 pixels, while the actual window size is ∼6 cm × 4 cm. The convective velocity of the flow was 4.5 cm s^{-1} in all of the experiments reported here. The images were taken at $T = 1.21$ and are in the region of self-similar development ($T > 1$) of the buoyancy mix. The mushroom-shaped structures are characteristic of Rayleigh–Taylor instability. These vortices are three-dimensional structures, with the vorticity field resembling that of a vortex ring. This is a predominantly irrotational flow, with most of the vorticity concentrated within the roll-up. Observations from the experiment of the axisymmetric nature of these

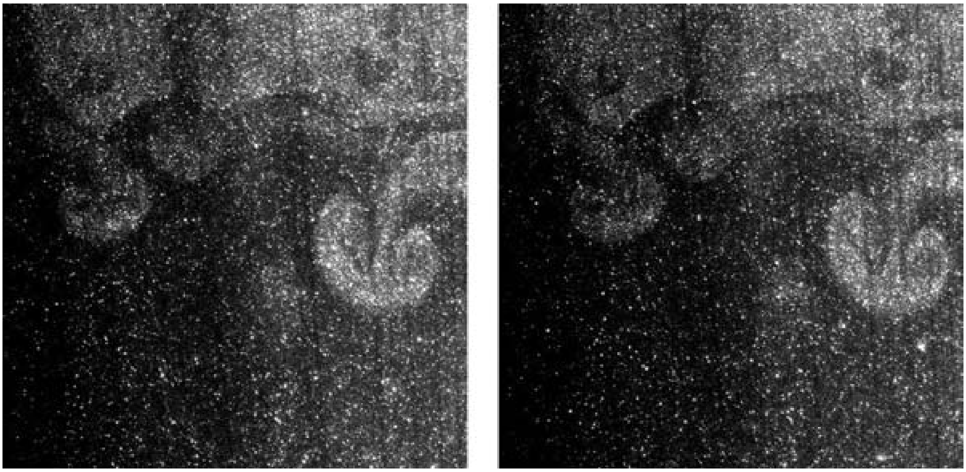

FIGURE 12. Two successive particle images showing mushroom-shaped structures characteristic of R-T instability.

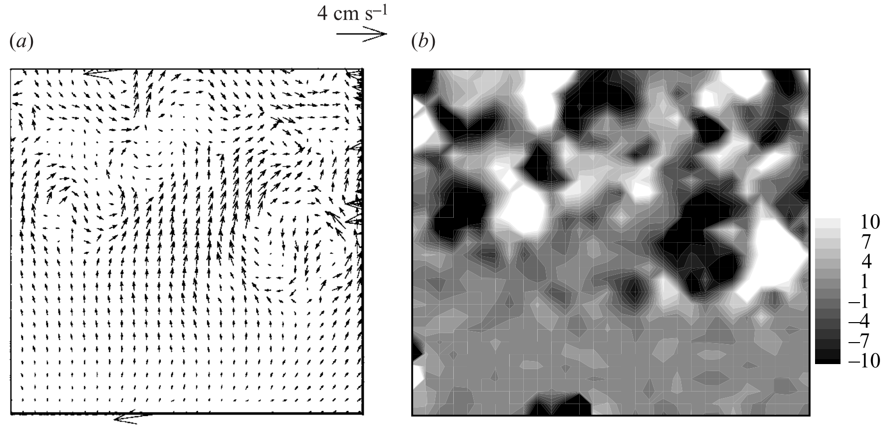

FIGURE 13. (*a*) Velocity vector field and (*b*) vorticity field obtained by cross-correlating the image files of figure 12.

mushroom structures imply isotropy between the streamwise and spanwise velocity components.

Figure 13(*a*) shows the velocity vector field (from which the mean convective velocity has been subtracted) obtained as a result of correlating the two greyscale images. A 16×16 pixel interrogation window was used to compute the vector fields. The corresponding out-of-plane z-vorticity component (in s^{-1}) is presented in figure 13(*b*). From the uncertainty in velocity measurements, the error in vorticity was determined to be $\sim \pm 0.05\,\mathrm{s}^{-1}$. Apart from a few bad vectors at the edge, the vector field captures the recirculating regions seen in the original images. The same is true for the vorticity field, where the two-dimensional slices of the recirculating zone show up as alternate regions of positive and negative vorticity.

The vorticity field seen in figure 13(*b*) is generated primarily through the baroclinic interaction of the density gradient and the pressure gradient (acceleration). For early stages in the instability development, the vorticity equation may be written as (Turner

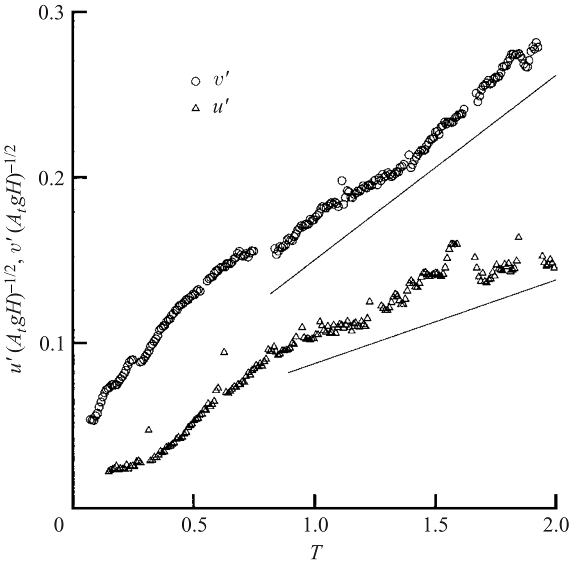

Figure 14. Centreline vertical and horizontal velocity r.m.s. as a function of non-dimensional time.

1980)

$$\frac{D\zeta}{Dt} = \zeta \cdot \nabla u + \nu \nabla^2 \zeta + \nabla p \otimes \nabla \left(\frac{1}{\rho}\right). \tag{25}$$

The first two terms on the right-hand side of the above vorticity equation indicate changes in vorticity ζ, produced by vortex line stretching and diffusion. The third term, unique to buoyancy driven flows, describes vorticity generation through misalignment of the local density gradient and the pressure gradient. During the initial stages of our experiment, the pressure gradient is the hydrostatic pressure introduced by gravity, and vorticity generation can occur when surfaces of constant density are displaced away from the horizontal. The initially sinusoidal vortex sheets evolve through localized stretching, before rolling up to form coherent vortices in the shape of mushrooms. Depending on the vortex sheet thickness, secondary instabilities (shear-driven or buoyancy-driven) may develop within the region of roll-up (e.g. the single-mode experiments of Waddell, Niederhaus & Jacobs 2001).

3.2. *Statistics*

From the low-resolution PIV experiments described earlier in this section and given in table 2, the centreline r.m.s. values of the vertical, v', and horizontal, u', velocity components at locations $0 < T < 1.8$ are shown as a function of time in figure 14. The v' values, after an initial period of exponential growth ($T < 0.5$), grow linearly with time in the self-similar region. (However, it is not clear if the condition for exponential growth of initial disturbances, $h_\lambda \ll \lambda$ is satisfied in these experiments.) The centreline vertical velocity normalized by $\sqrt{A_tgH}$ reaches a peak value of 0.28 at $T = 1.9$. The vertical velocity at the centreline can be related to the mix width of (1) by

$$v' = \frac{dh}{dt} = 2\alpha A_t g t. \tag{26}$$

Note that (26) is valid only in the self-similar region of the flow. Thus, from the

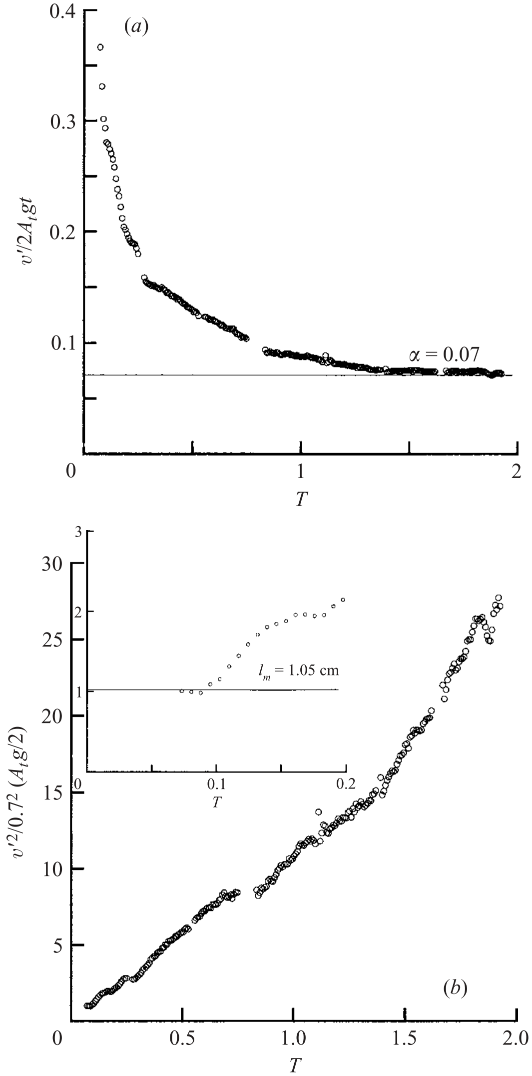

FIGURE 15. (*a*) $\alpha = v'/(2A_t g t)$ at the centreline plotted as a function of T. (*b*) $l_m = v'^2/(0.7^2 A_t g/2)$ at the centreline plotted as a function of T. Inset shows l_m close to the splitter plate.

time evolution of v', we can determine the growth constant α by computing the ratio $v'/2A_t g t$. This ratio is plotted as a function of the non-dimensional time in figure 15(*a*). The saturation of α at late time to a constant value of 0.07 suggests that the flow reaches self-similarity in these experiments. This is an interesting result, as in the past we obtained the same value for α of 0.07 in this experiment (Snider & Andrews 1994) by measuring the mix width h (based on the 5% and 95% threshold for the volume fraction) directly and relating it to α through (1). Therefore, by using (26) and obtaining $\alpha = 0.07$ from the centreline value of v', we imply that the expansion of the mix is driven by velocity fluctuations that occur across the whole mix and not just the edge. This characterization is supported by observations of the mixing layer, shown in figure 2, where large-scale structures span the mix and dominate the velocity fluctuations. As a result, many of the statistics presented in this work remain

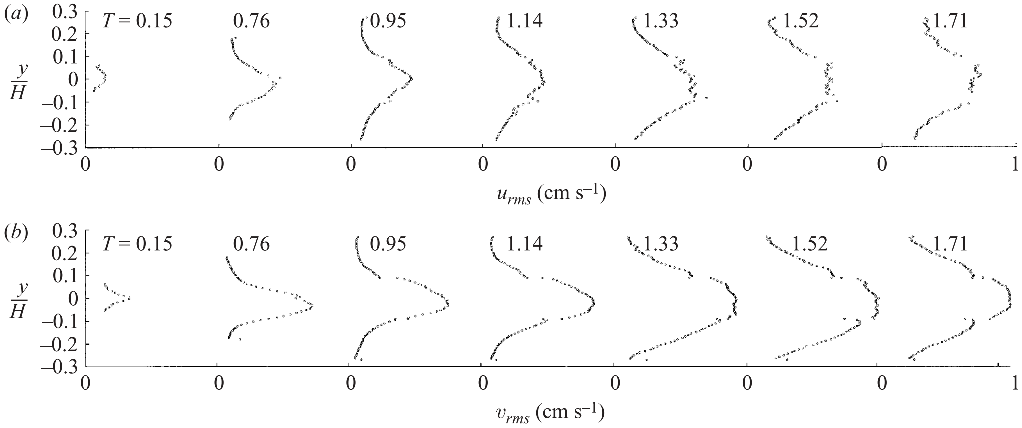

FIGURE 16. (a) u' profiles at different T-locations; (b) v' profiles at different T-locations.

practically constant across the mix. Spectral analysis of the velocity fluctuations later provides further support for this interpretation of the mix dynamics.

At early times, we may expect a single wavelength to dominate the dynamics. The centreline vertical velocity may then be approximated by the terminal velocity (Andrews & Spalding 1990), a natural extension of Layzer's (1955) terminal velocity formulation for $A_t = 1$,

$$v' \sim 0.7\sqrt{A_t g l_m/2}, \tag{27}$$

where l_m is the dominant growing wavelength. We may then determine the value of l_m in this flow by plotting $v'^2/(0.7^2 A_t g t/2)$ in figure 15(b). The value of l_m thus obtained from the flat region close to the splitter plate (at $0.07 < T < 0.12$) was 1.05 cm (figure 15(b) inset); a peak in the velocity spectral data, close to the inlet, around this value further confirms the presence of a dominant wavelength at $l_m \sim 1.05$ cm (§ 3.3). The appearance of the second plateau between $T \sim 0.15$ and $T \sim 0.2$ is believed to be the result of pairing of these structures. At late time, the value of l_m reaches a maximum of ~ 27 cm comparable to the channel depth of 30 cm, although it is no longer accurate to characterize the dynamics in terms of a single wavelength. Not surprisingly, the single-mode dynamics in this experiment are restricted to very early stages of the R-T development.

The cross-stream profiles of horizontal and vertical velocity fluctuations are shown in figures 16(a) and 16(b), respectively. The velocity axes are retained in dimensional coordinates to give a sense of the relative magnitudes of the peak values as they evolve in time. Vertical velocity fluctuations dominate over the horizontal velocity component and provide most of the transport of mass, momentum and energy. The figure indicates that for $T > 0.76$, the velocity profiles evolve in a shape-preserving manner and will collapse onto a single curve when normalized by the appropriate variables.

We normalize with a saturation velocity defined by $u_\infty = 0.7\sqrt{A_t g h_x/2}$, where h_x is the local mix-width computed from $h_x = \alpha A_t g t^2$ with $\alpha = 0.07$. Then, u_∞ and h_x are chosen as the self-similar scales and used to normalize the cross-stream velocity profiles in figure 16. The results for the horizontal and vertical velocity fluctuations are shown in figures 17 and 18, respectively, and show a good collapse for all T-locations except $T = 0.76$ where the flow may not be fully self-similar. The vertical velocities expressed in terms of the saturation velocity have a peak around 1, showing that

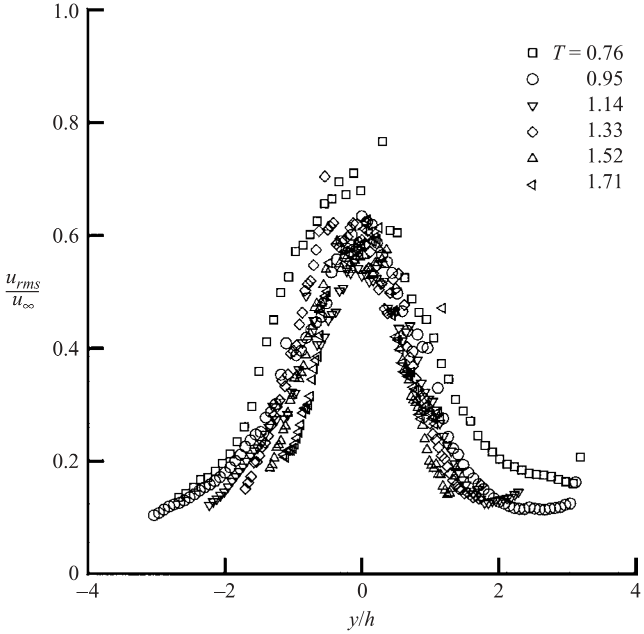

FIGURE 17. u' profiles at different T-locations expressed in self-similar units.

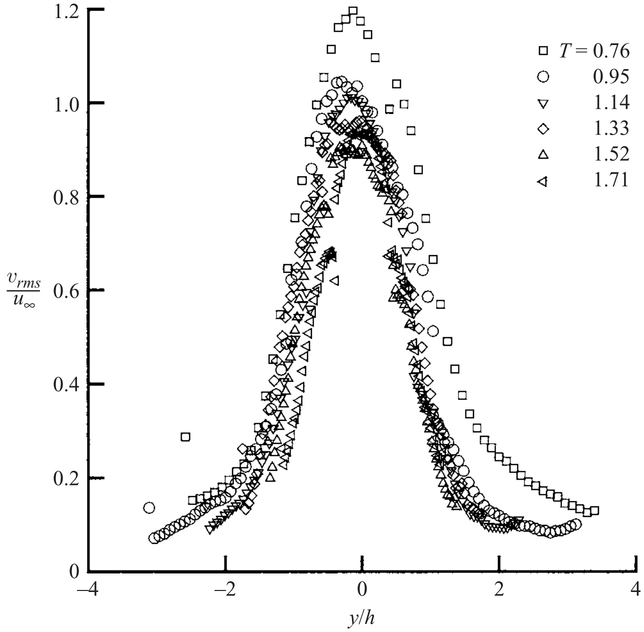

FIGURE 18. v' profiles at different T-locations expressed in self-similar units.

this choice of the self-similar variable is appropriate and physically meaningful. Since there is no shear in this experiment, v' dominates over u' everywhere. This dominance decreases with downstream distance from a ratio ~ 2 close to the splitter plate, to a ratio of ~ 1.6 as the structures become more three-dimensional. Furthermore, by $T = 1.21$ the ratio v'/u' is almost constant across the mixing layer (figure 19),

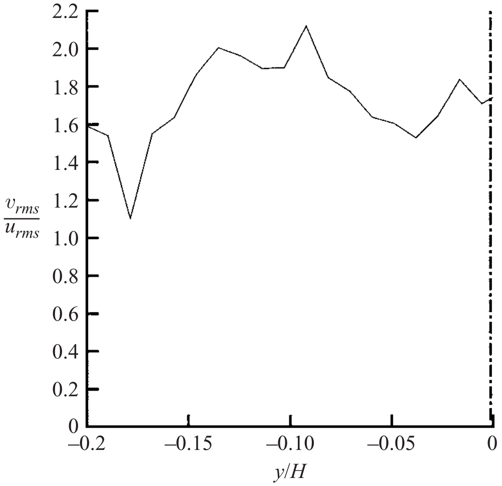

FIGURE 19. Ratio of v'/u' across the mix at $T = 1.21$

suggesting an existing equilibrium between the u'- and v'-kinetic energy production terms everywhere.

J. R. Ristorcelli (personal communication 2001) suggested that the large-scale anisotropy between u'^2 and v'^2 can also be characterized through the normalized anisotropy tensor, b_{ij}. A discussion on the geometry of the small scales is deferred until § 3.3. Following Pope (2000), the anisotropy tensor is defined as

$$b_{ij} = \frac{\langle u_i u_j \rangle}{\langle u_k u_k \rangle} - \tfrac{1}{3}\delta_{ij}, \tag{28}$$

where $\delta_{ij} = 1$ for $i = j$, 0 otherwise, and $\langle u_k u_k \rangle$ is twice the kinetic energy. Thus, this is the deviatoric part of the Reynolds stress tensor normalized by the kinetic energy term. Pope (2000) shows that the anisotropic stress tensor is responsible for the transport of turbulent momentum. In a R-T mix, the cross-correlation term $\langle u'v' \rangle$ is negligible since the mushroom-shaped structures have left–right symmetry about the centre, so $u'v'|_{right} = -u'v'|_{left}$. Similarly, for u- and w-components, $\langle w'v' \rangle$ and $\langle w'u' \rangle \sim 0$. Thus,

$$\langle u_i u_j \rangle = \begin{pmatrix} \langle u'^2 \rangle & 0 & 0 \\ 0 & \langle v'^2 \rangle & 0 \\ 0 & 0 & \langle w'^2 \rangle \end{pmatrix}. \tag{29}$$

In (29), $\langle u'^2 \rangle$ and $\langle v'^2 \rangle$ are measured, and $\langle u'^2 \rangle = \langle w'^2 \rangle$ is taken from axisymmetry of the coherent structures. For isotropic turbulence, $\langle u_i u_i \rangle / \langle u_k u_k \rangle = 1/3$ and so $b_{ii} = 0$. Also, $-1/3 \leqslant b_{ij} \leqslant 2/3$, where the upper and lower limits represent one-dimensional and two-dimensional distributions of turbulent kinetic energy, respectively. Thus, b_{ij} characterizes the geometry of the turbulence, independent of the amplitude of the fluctuations.

Figures 20(*a*) and 20(*b*) are plots of the anisotropy tensor across the mix at $T = 0.07$ and $T = 1.21$, respectively, where b_{uu} corresponds to the horizontal velocity component, and b_{vv} corresponds to the vertical velocity component. At both times, near the centre of the mix, most of the transport appears to be in the vertical direction. Once again, we see that the statistics are reasonably constant across the mix at $T = 1.21$. It appears that at both locations $b_{ii} \rightarrow 0$ near the edges of the mix,

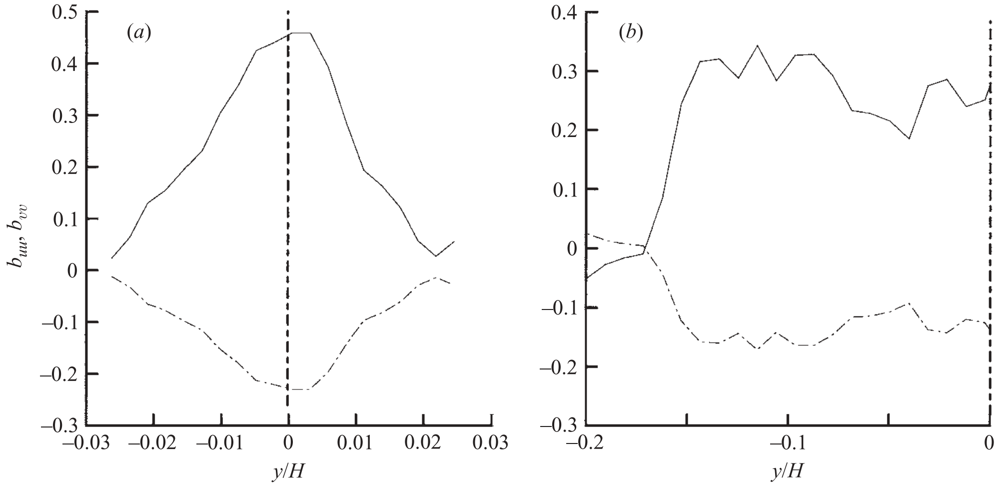

FIGURE 20. Profiles of the anisotropy tensor across the mix at (*a*) $T = 0.07$, and (*b*) $T = 1.21$. ——, b_{vv}; —·—, b_{uu}.

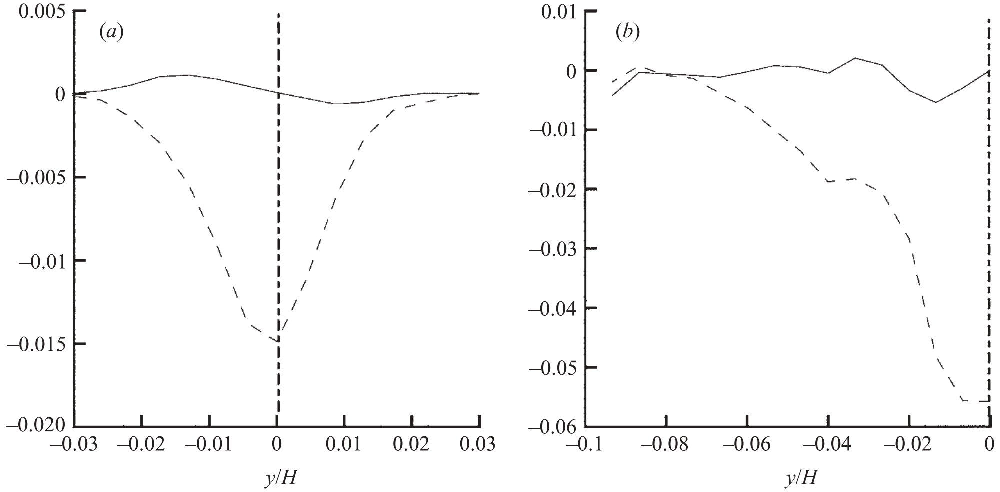

FIGURE 21. Profiles of $\overline{\rho' u'}/\Delta\rho(A_t g H)^{1/2}$ (solid line), and $\overline{\rho' v'}/\Delta\rho(A_t g H)^{1/2}$ (dashed line) across the mix at (*a*) $T = 0.07$ and (*b*) $T = 1.21$.

which is attributed to the decay of turbulent fluctuations in this region rather than any inherent local isotropy. At $T = 0.07$, the drop off near the edges is more gradual, suggesting the presence of a viscous diffusive layer. Thus, it appears that the mix at the end of the splitter plate consists of a central region where buoyancy dominates padded by viscous layers at both the top and bottom. The geometry of the small scales is discussed in the following section.

The primary transport term in an R-T flow is the mass flux term $\langle \rho' v' \rangle$, which can be computed from PIV-S data. The results normalized by $\Delta\rho(A_t g H)^{1/2}$ are shown for $T = 0.07$ and $T = 1.21$ in figure 21. At both locations, $\langle \rho' u' \rangle$ is negligible, owing once again to the left–right symmetry of the mushroom-shaped structures, but $\langle \rho' v' \rangle$ has a peak that increases in magnitude with distance downstream. The vertical mass flux is negative because a packet of fluid that is lighter than its neighbouring fluid particles

($\rho' \equiv \rho - \overline{\rho} < 0$) will travel upwards with a velocity $v'(v' > 0)$ and vice versa, giving a negative correlation between ρ' and v'. These fluxes are more commonly normalized by $\Delta\rho u_\infty$ (Ramaprabhu & Andrews 2003). These results should be interpreted with caution away from the centreline, where θ_{PIVS} reverts to a two-fluid value.

3.3. *Spectra*

To study the structure of small scales, velocity and density spectral data are presented in this section in the wavenumber domain. The velocity spectra were computed by extracting a velocity time series at the centreline at certain spatial locations, and then calculating the power associated with the (mean-subtracted) signal in the Fourier domain. To compare with the wavenumber spectra obtained directly from spatial variations in the velocity field, the temporal data have been converted to spatial data first using the Taylor hypothesis, and the spectra then computed in the wavenumber domain. Similarly, density fluctuation spectra have been computed from the temperature time series (converted to spatial data) obtained from thermocouple measurements. The density data obtained from the equation of state, are first non-dimensionalized to give $\rho^* = (\rho - \rho_2)/(\rho_1 - \rho_2)$. Then, the scalar energy spectra are computed using the equation

$$E_{\rho'}(k) = \frac{2\Delta x}{N}\left|\sum_{i=0}^{N-1} \rho_i^* \exp(2\pi j k x_i)\right|^2, \tag{30}$$

where N is the number of samples, $\Delta x = U\Delta t$ is the sampling interval, and $j = \sqrt{-1}$. Thus, the scalar energy spectrum is the wavenumber representation of B_0, i.e. $\int_0^\infty E_{\rho'}(k)\,\mathrm{d}k = B_0$.

The non-dimensional energy spectra of density fluctuations $E_{\rho'}(k)H^{-1}$, at $T = 0.034 (x \sim 1\,\text{cm})$ is shown in figure 22(*a*). The corresponding compensated energy spectrum $k^4 E_{\rho'}(k)$ (normalized as $k^4 E_{\rho'}(k)H^3$) is plotted in figure 22(*b*). The factor k^4 is used to illustrate regions with a slope of —4, which will appear horizontal in the compensated spectrum. Inspection of figure 22(*b*) shows a region of zero slope toward the higher wavenumbers, an exponential —4 collapse that corresponds to the presence of a viscous diffusive layer at the start of the mix formed in the wake of the splitter plate (Corrsin 1951). At this early time, no equilibrium has been achieved between the production and dissipation terms as evidenced by the absence of an inertial range. From figure 22(*a*), it is evident that most of the energy is instead concentrated evenly in the low-wavenumber region of the spectrum ($kH < \sim 20$).

The corresponding velocity spectra $E_{u'}(k)$ and $E_{v'}(k)$ at $T \sim 0.07$ normalized by $H^2 A_t g$ are shown in figure 23 and have a similar two-region structure: a flat region at the low-end of the wavenumber range followed immediately by a steep (slope ~ -4) dissipative high-wavenumber region. Similar to the density spectra, there is a peak around $kH \sim 20$ corresponding to a dominant wavepacket. Without this initial dominant wavepacket, the k^{-4} fall-off would have started earlier, and the dip seen just before $kH \sim 20$ is indicative of this collapse. Consistent with the profiles of $\langle u'^2 \rangle$ and $\langle v'^2 \rangle$ seen earlier, vertical fluctuations dominate, particularly at low wavenumbers, which make up most of the energy. It is believed from these measurements that for this experimental set-up, the velocity spectrum, rather than the density spectrum, at the end of the splitter plate represents the true initial perturbation to the flow. This is because velocity perturbations are shed from the splitter plate, which lead to the formation of density perturbations in the wake. This is in contrast with Richtmeyer–Meshkov experiments where the initial perturbation is provided directly to the density interface.

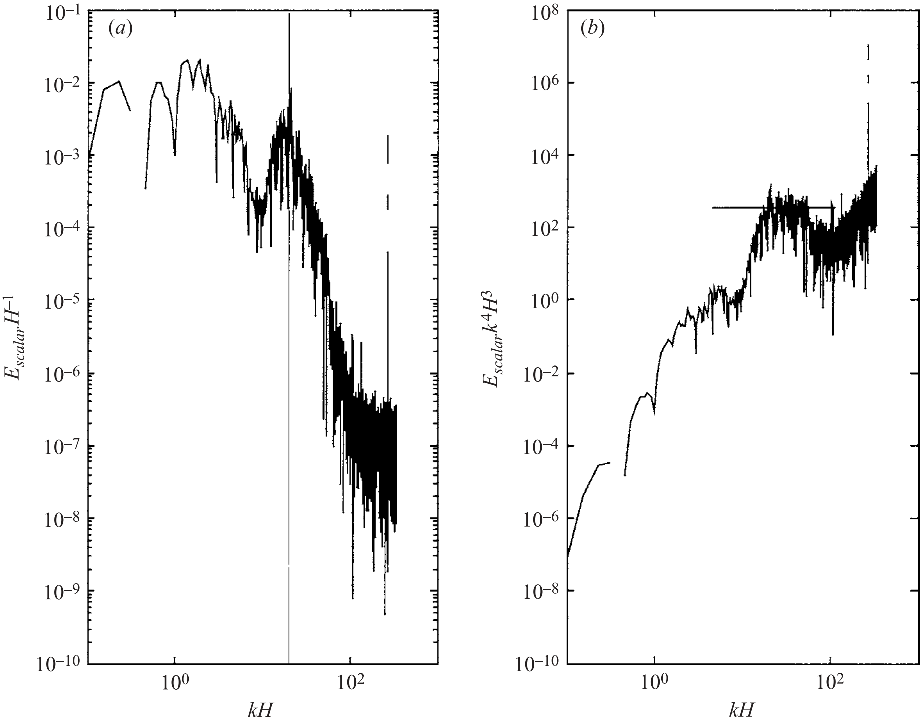

FIGURE 22. Density fluctuation spectrum (*a*) at $T = 0.034$ at the centreline. The dashed line represents $kH = 20$. (*b*) Compensated fluctuation spectrum $k^4E(k)$. Solid line represents the horizontal.

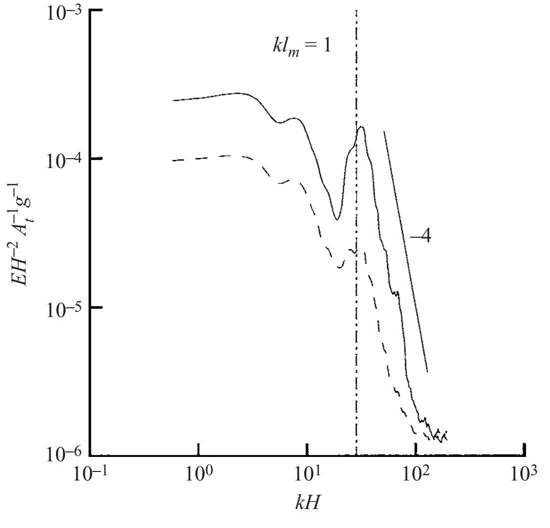

FIGURE 23. Frequency velocity spectra at $T = 0.07$ at the centerline. The dashed line represents $kH \sim 20$. ——, v'; – – –, u'.

The velocity spectra obtained here may be used to initialize numerical simulations of Rayleigh–Taylor flows that are often initialized with density perturbations. Such simulations of our experiment are currently underway, and should do much to resolve the differences in α between experiments and numerical simulations. We note

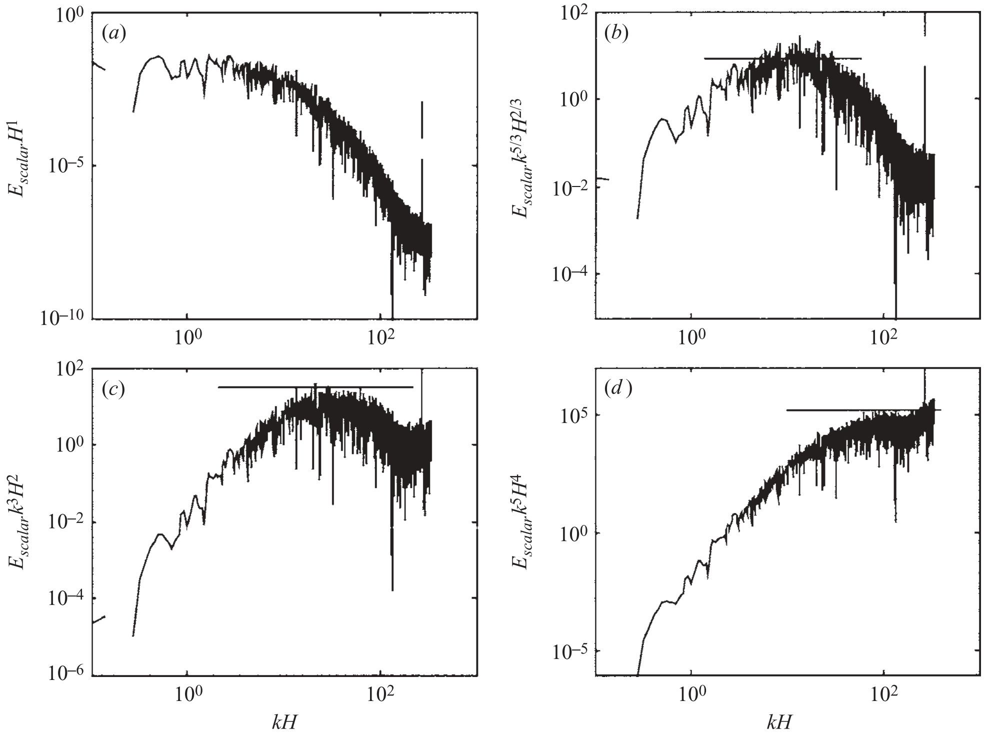

FIGURE 24. (*a*) Centreline density fluctuation spectrum $E(k)$ at $T = 1.008$ and compensated fluctuation spectra $k^m E(k)$ where (*b*) $m = 5/3$, (*c*) $m = 3$, and (*d*) $m = 5$. Solid line represents the horizontal.

the work of Dalziel *et al.* (1999), who used initial velocity spectra from their barrier experiments, and report good quantitative agreement in the large-scale measures such as the mix width. The perturbations in our experiment are primarily two-dimensional owing to small-scale wake shedding off the end of the splitter plate, with short-wavelength modes (ripples) in the third horizontal direction across the flow. As mentioned previously, the dashed line indicating $l_m = 1.05\,\mathrm{cm}$ corresponds closely to a peak in the energy spectra, showing that the early-time dynamics shown here are dominated by a single wavelength that may also be conveniently represented in a numerical simulation.

Figures 24(*a*) and 25(*a*) show the density fluctuation spectra at times $T = 1.008$ and $T = 2.086$, respectively. The compensated energy spectra $k^m E_{\rho'}(k)$ (normalized as $k^m E_{\rho'}(k) H^{m-1}$) are also plotted in figures 24(*b*) and 25(*b*) $m = 5/3$, (*c*) $m = 3$ and (*d*) $m = 5$. Figures 24 and 25 are snapshots of the density fluctuation spectra at early and late stages of the self-similar evolution. At each stage, there appear to be four distinct regions in the fully developed scalar spectrum (Wilson & Andrews 2002): (i) an energy containing range; (ii) an inertial subrange with nearly a $-5/3$ slope; (iii) a viscous-diffusive subrange with a -3 slope; and (iv) a steeper diffusion dominated region with a -5 slope. Figure 25 shows that with time, the viscous-diffusive layer is relegated primarily to the smaller scales where the energy cascade is due to stretching of fine-scale structures by the local velocity fields. Finally, at $T = 2.08$, the -5 region occupies a very small portion of the spectrum. This process is accompanied by buoyancy-driven filling in (owing to the development of the mushroom-shaped coherent structures) of the $-5/3$ portions of the spectra. Since $Re = 2h\dot{h}/\nu \propto t^3$ in this

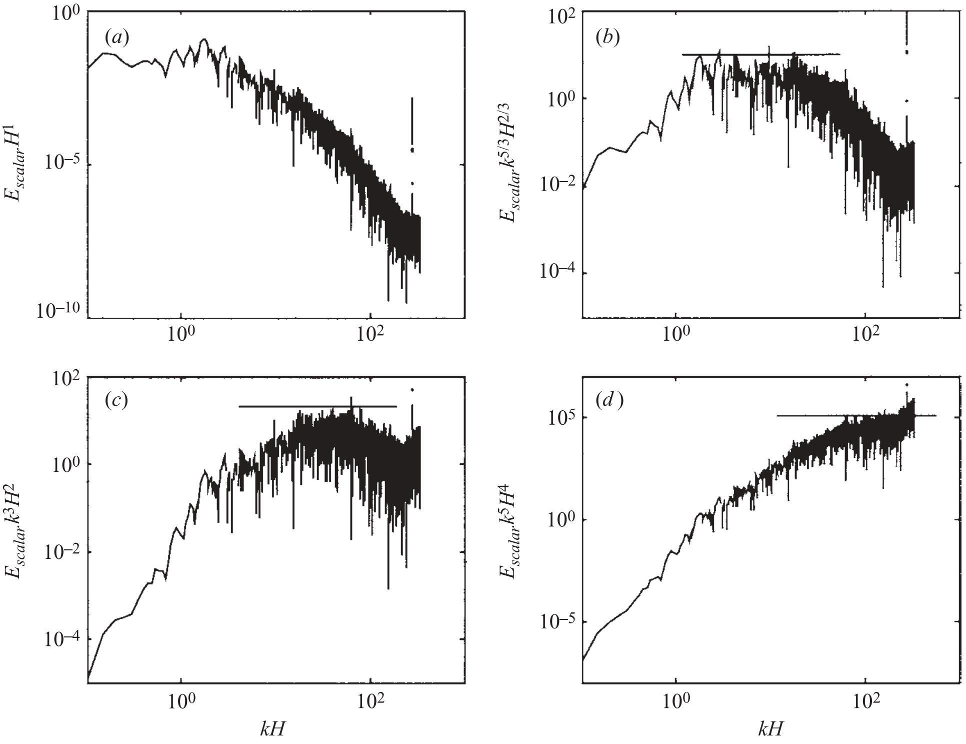

FIGURE 25. (a) Centreline density fluctuation spectrum $E(k)$ at $T = 2.08$ and compensated fluctuation spectra $k^m E(k)$ where (b) $m = 5/3$, (c) $m = 3$, and (d) $m = 5$. Solid line represents the horizontal.

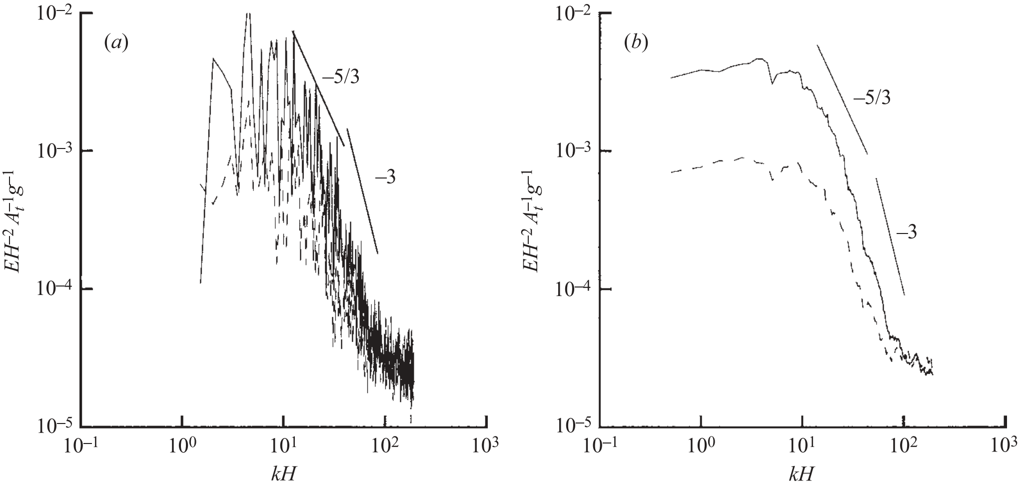

FIGURE 26. Frequency velocity spectra at the centreline at $T = 1.21$: (a) raw spectra and (b) spectra smoothed using a window-averaging process. ——, v'; – – – u'.

flow, the inertial range increases in width rapidly, spanning almost two decades of frequencies by $T = 2.08$.

In figure 26(a), the velocity spectrum at $T \sim 1.21$ also shows an inertial range with approximately a $-5/3$ slope and a dissipative range with a -3 slope. To elucidate the slopes in the velocity spectra, a moving window-averaging process was used that preserved the integral of $E_{u'}(k)$ and $E_{v'}(k)$ to within 1%. Figure 26(*b*) presents the results of this smoothing process, with a window size of 20 points. Again, at the large scales there is considerable anisotropy between the horizontal and vertical components. However, at higher wavenumbers, there is a convergence of energy associated with the horizontal and vertical velocities, indicating a tendency towards isotropy at these scales. Although we capture up to two decades in the wavenumber domain, we do not completely resolve the dissipative scales, as evidenced by the saturation (flattening) at large wavenumbers. From (6), $Re_x \sim 1450$ at $T \sim 1.21$. The corresponding Kolmogorov time scale is (Tennekes & Lumley 1972)

$$\tau_k = \mathscr{T} Re_x^{-1/2} = 0.052\,\mathrm{s}. \tag{31}$$

Here, τ_k is the Kolmogorov time scale and $\mathscr{T}$ is the integral time scale ($=2h_x/U$). Thus, at a sampling rate of 30 Hz ($\Delta t = 0.03\,\mathrm{s}$), the corresponding Nyquist limit ($\sim 0.026\,\mathrm{s}$) is not satisfied. Furthermore, there is also some spatial averaging due to the finite size of the PIV window, which could contribute to a smearing of the signal at higher frequencies.

In the self-similar region of the flow ($T > 1$), an equilibrium is achieved between the production and dissipation terms of the kinetic energy equation. This equilibrium manifests itself as the $-5/3$ region in the spectrum. The universal inertial range spectrum is given by (Tennekes & Lumley 1972)

$$E(k) = A\varepsilon^{2/3}k^{-5/3}, \tag{32}$$

where ε is the kinetic energy dissipation rate and A is a universal constant. From the u' and v' velocity spectra, the net three-dimensional kinetic energy spectrum may be computed by assuming isotropy between u'- and w'-components of the velocity fluctuations. In (32), A was determined through a curve fit of the experimental data to $E(k)$ to be ~ 5 ($A \sim 1.5$ for most turbulent flows, Tennekes & Lumley 1972). In the above, ε was determined from the integral of $\mathrm{D}(k)$ the dissipation spectrum given by

$$\mathrm{D}(k) = 2\nu k^2 E(k), \tag{33}$$

where ν is the viscosity and $\varepsilon = \int \mathrm{D}(k)\,\mathrm{d}k$. Correspondingly, the production spectrum $P(k)$ can be written as

$$P(k) = \frac{2\pi B}{A^{1/2}}\frac{S^2}{\varepsilon^{1/3}}k^{-2/3}E(k), \tag{34}$$

where S is the dominant strain rate in the flow ($S = u/l$, where u and l are the velocity and length scales given by $u = v'$ and $l = u^3/\varepsilon$, respectively, and B is another universal constant). By fitting the experimentally measured $P(k)$ to (34), B was determined to be 0.6 ($B \sim 0.3$ for a typical turbulent flow, Tennekes & Lumley 1972). The difference between the measured values of A and B from those obtained from other flows is believed to be due to the moderate values of Re employed in the current work. Thus, $P(k)$ represents the production of kinetic energy primarily due to straining of eddies by successively larger eddies. Figure 27 is a plot of the above defined spectra for $T = 1.21$. Production is dominant at low wavenumbers, and dissipation is dominant at high wavenumbers. The intermediate region (enclosed by the solid lines), where $P(k)$ and $D(k)$ intersect, is thus the inertial subrange. In this subrange, the energy transfer spectrum $T(k) = (2\pi/A^{3/2})kE(k)s(k)$ has a zero slope indicating constant energy flux.

Wavenumber power spectra were also obtained by taking velocity data points along a vertical slice of the two-dimensional velocity field. The higher wavenumbers

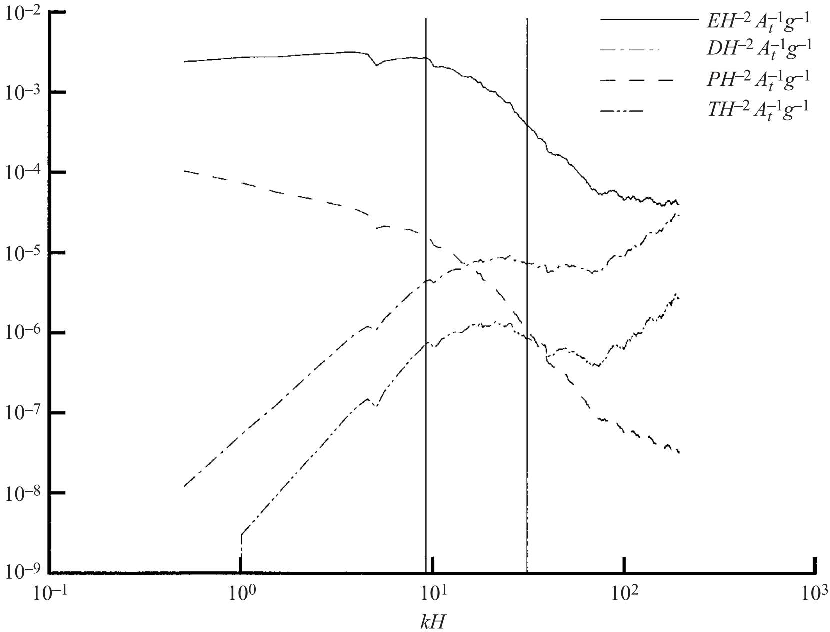

FIGURE 27. Spectra of total kinetic energy $E(k)$, production $P(k)$, dissipation $D(k)$, and transfer $T(k)$ at $T = 1.21$ at the centreline.

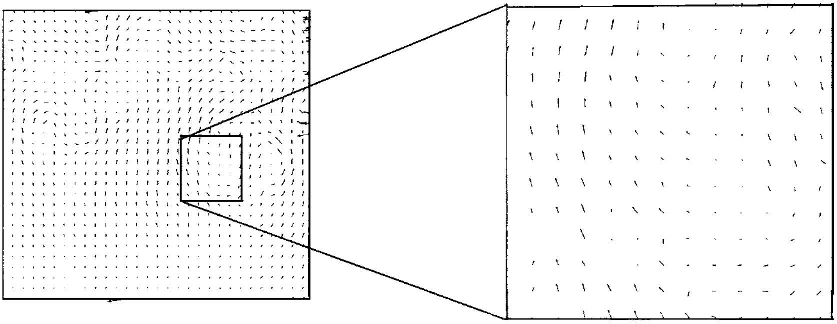

FIGURE 28. Velocity field from figure 13(a) processed through the iterative-PIV technique.

were captured by repeating the experiment, with the PIV camera placed much closer to the channel. This reduced the physical size of the window from 6 cm × 4 cm to 3 cm × 2 cm, thus doubling the spatial resolution. A further increase in resolution was obtained by using an iterative PIV technique (Scarano & Riethmuller 1999), an approach similar to that used in multi-grid numerical simulations. In the first iteration, the displacement vector is computed to integer accuracy. The interrogation window size is then halved and the integer displacement is used to search for a correlation peak, thus giving a velocity vector that is of subpixel accuracy. Figure 28 shows the vector field of figure 13(a), but processed using the iterative approach, giving twice the resolution. Thus, with both refinements we are able to achieve a four-fold improvement in resolution, and we can capture turbulence length scales as small as 0.03 cm.

Figures 29(a) and 29(b) are plots of the wavenumber spectra at $T = 0.07$ and 1.21, obtained from the above process. The structural properties are similar to the

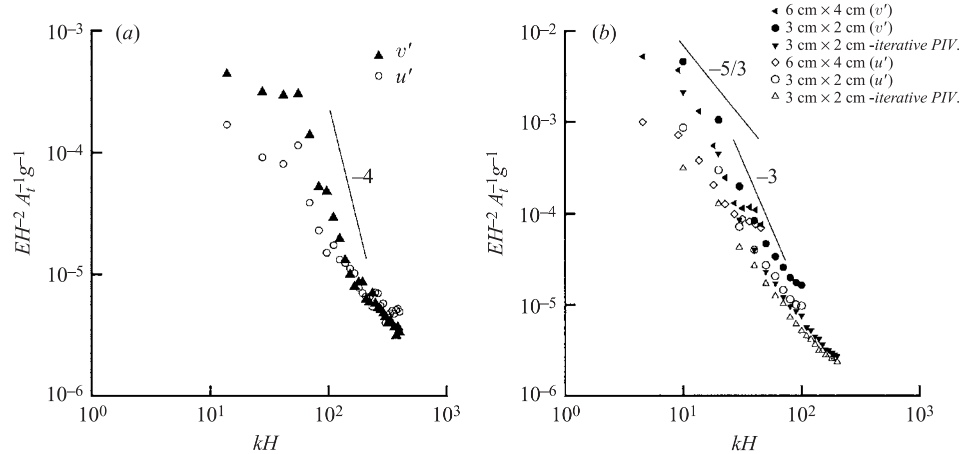

FIGURE 29. Wavenumber velocity spectra at the centreline at (*a*) $T = 0.07$ and (*b*) $T = 1.21$.

spectra obtained from time series data: anisotropy at the large scales and a tendency towards isotropy at the smaller scales. At $T = 0.07$, the wavenumber spectrum shows a flat top and a steep dissipative range at high wavenumbers. The spatial resolution at this Reynolds number is sufficient to capture the Kolmogorov scales. Also, at $T \sim 1.21$, there is a distinct inertial range with the $-5/3$ slope. For the u' and the v' velocities, the spectra were constructed by overlaying the individual spectra from each wavenumber range. The tailing off seen at the end of each of these spectra is due to noise saturation at that resolution. Thus, by coming in closer and applying the iterative PIV technique, both the resolution and the accuracy of the measured wavenumber spectra have been improved.

From the results, it is evident that buoyancy forcing at small Atwood numbers does not affect the formation of a $-5/3$ inertial range, in accordance with the classical Obukhov–Corrsin theory for turbulent scalar fluctuations (Obukhov 1949; Corrsin 1951). The scaling argument proposed by Zhou (2001) for the velocity spectra of a Rayleigh–Taylor flow is extended here to scalars. Zhou argues that the kinetic energy dissipation is a function of the timescale of decay of triple velocity correlations, $\tau(k)$,

$$\varepsilon \sim \tau(k) k^4 E^2(k), \tag{35}$$

where $E(k)$ is the kinetic energy spectrum, k is the wavenumber, and the exponents in the above equation are obtained from dimensional analysis. In the absence of external forcing on the energy containing eddies (e.g. homogenous, isotropic turbulence), τ may be chosen as the timescale of nonlinear interactions among the energetic modes.

$$\tau(k) = [k^3 E(k)]^{-1/2}. \tag{36}$$

Substituting for (36) in (35), the classical Kolmogorov form of the energy spectrum is recovered:

$$E(k) \sim \varepsilon^{2/3} k^{-5/3}. \tag{37}$$

In the presence of external buoyancy forcing, the governing timescale is supplied by gravity. Thus, $\tau_{RT} = (kA_t g)^{-1/2}$, giving (Zhou 2001)

$$E_{RT}(k) \sim (gA_t)^{1/4} \varepsilon^{1/2} k^{-7/4}. \tag{38}$$

The constant of proportionality in (38) was determined to be ~ 3 from our experimental velocity data. An extension of the above argument may be proposed for

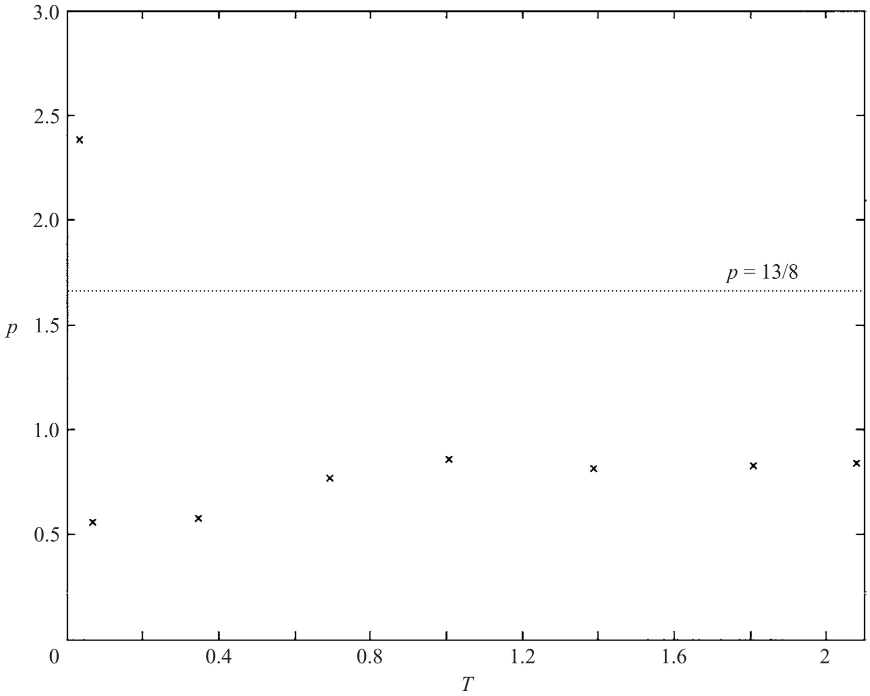

FIGURE 30. Time evolution of exponential curve-fit index, p, for centreline temperature measurements.

buoyancy forcing of the scalar fluctuation spectrum. The dissipation of scalar variance is given by (Tennekes & Lumley 1972)

$$N \sim k^2 E^{scalar}(kE_{RT})^{1/2}. \tag{39}$$

Substituting for $E_{RT}(k)$ from (38), we obtain

$$E_{RT}^{scalar} \sim N(A_t g)^{-1/8} \varepsilon^{1/4} k^{-13/8}, \tag{40}$$

giving a power law close to the $-5/3$ observed in the present experiments. For $T \sim 1.008$, the constant in (40) was determined from our data to be ~ 1. Thus, it appears that the buoyancy forcing does not significantly alter the power law of the inertial range.

The spectral structure of temperature (density) fluctuations at each time can be quantified through an exponential curve fit, $E(k) \sim \mathrm{e}^{-p}$. The best fit to the data is obtained by performing a Nelder–Mead simplex direct search (Nelder & Mead 1965) in p-space by minimizing the function $E(k) - \mathrm{e}^{-p}$. For $Re \to \infty$, p should $\to 13/8$ for density fluctuations in R-T flows. Figure 30 is a time history of p and shows that this asymptotic value is never reached owing to the finite values of Re in this experiment. At early times, $p \sim 2.5$ is highest owing to the presence of the viscous-diffusive layer with an exponential drop-off. However, the onset of self-similarity ($T \sim 1.008$) is clearly marked by the attainment of a constant value by p ($\sim$0.85). This implies that the structure of the scalar spectra is preserved in the self-similar regime even as it contains regions where the slope is not $-13/8$. These are primarily the energy-containing scales and the diffusive scales. At high enough Re, it is expected that these scales will occupy a much smaller percentage of the spectral width giving a value for p approaching $13/8$.

Taylor length scale, λ_x	0.29 cm
Taylor length scale, λ_y	0.62 cm
Vertical velocity scale, v'	0.82 cm s^{-1}
Horizontal velocity scale, u'	0.45 cm s^{-1}
Taylor Reynolds number, $Re_{\lambda y}$	60
Kolmogorov length scale, η	0.027 cm

TABLE 3. Taylor scales at $T = 1.21$.

4. Taylor microscales

More significant than the Kolmogorov scales are the Taylor microscales associated with the local strain rate, and can be directly obtained from the turbulent velocity fluctuations. The Taylor length scales, λ_u and λ_v, associated with the horizontal and vertical velocity fluctuations are given by

$$\lambda_u(t) = \left[-\tfrac{1}{2}f''(0,t)\right]^{-1/2}, \quad \lambda_v(t) = \left[-\tfrac{1}{2}g''(0,t)\right]^{-1/2}, \tag{41}$$

where $f(r,t)$ and $g(r,t)$ are the non-dimensional autocorrelation functions given by

$$f(r,t) = \langle u(x+r,t)u(x,t)\rangle / \langle u^2\rangle,$$
$$g(r,t) = \langle v(x+r,t)v(x,t)\rangle / \langle v^2\rangle.$$

Thus, the Taylor microscale is the r-intercept of the osculating parabola $f(r)$ at $r = 0$ (Pope 2000).

From the velocity data, a point at the centre of the mix was picked, and its autocorrelation function in space was computed. This process was repeated for other datapoints in the vicinity, and the mean Taylor length scale was determined. A histogram of the Taylor scales also showed a peak around the mean value. Like much of the velocity statistics described in § 3.2, it was found that the Taylor scales did not vary significantly across the mix. Thus, we present only the centreline values in the following.

The results are presented in table 3, along with the Kolmogorov scales for comparison. The Taylor scales in space show a tendency toward anisotropy with a λ_y/λ_x ratio approaching a value of 2. Cook & Zhou (2002) in their DNS simulations report a ratio of 1.4 at $T > 2.5$ (for $\rho_2/\rho_1 \sim 3$). Furthermore, the Taylor microscales are approximately 10–20 times the size of the Kolmogorov scales. Taking the velocity scale associated with the Taylor length scales to be the r.m.s. of vertical velocity fluctuations, a Taylor scale Reynolds number may be computed for the present experiment as

$$Re_\lambda = \frac{\lambda v'}{\nu} = 60. \tag{42}$$

This value is less than the threshold for mixing transition for turbulent flows ($Re_\lambda \sim 100$) and is expected to cross this value further downstream. However, we observe self-similarity has been achieved in these experiments as is evidenced by the p.d.f.s, spectra, and velocity profiles (for $T > 1$), even though our Taylor Reynolds number of 60 is less than the value of 100 suggested (Dimotakis 2000) for mixing transition. Thus, even at low Atwood numbers, there is surely a differential straining of eddies in the direction of gravity, resulting in anisotropy of velocity fluctuations at all but the smallest scales.

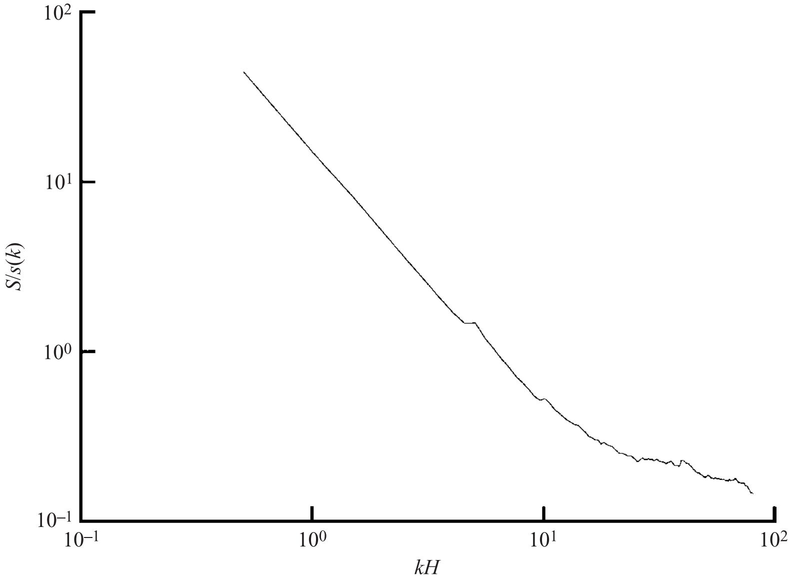

FIGURE 31. Spectra of $S/s(k)$ showing tendency toward isotropy at higher wavenumbers for the centreline velocity spectra.

This tendency toward anisotropy may be quantified by the local (in wavenumber space) strain rate. For any eddy of size $2\pi/k$, with a characteristic velocity scale defined as $[kE(k)]^{1/2}$, the characteristic strain rate can be defined as (Tennekes & Lumley 1972)

$$s(k) = \frac{(kE(k))^{1/2}}{2\pi/k} = \frac{(k^3E(k))^{1/2}}{2\pi}. \tag{43}$$

Thus, the local strain rate increases with decreasing eddy size, so that the smallest eddies undergo the severest straining. Following Tennekes & Lumley (1972), taking the time scale $1/s(k)$ to represent the time required to return to isotropy once the strain field is removed, the eddies with large k are quickest in their realignment. So the non-dimensional paramater $S/s(k)$, where S is the mean strain rate, characterizes the degree of isotropy (large $S/s(k) \rightarrow$ anisotropy). $S/s(k)$ is plotted for the velocity spectrum at $T \sim 1.21$ in figure 31 and shows anisotropy at all but the smallest scales. This is consistent with the picture depicted by the velocity spectra and Taylor microscales.

5. Energy budget

Following Youngs (1994), from our simultaneous measurements of velocity and density fields, the net kinetic energy dissipation from the initial state of the flow is computed. The initial potential energy PE_i, associated with the flow, is calculated assuming a stepfunction at $z = H/2$ for the density profile at $T = 0$. Thus,

$$PE_i = \int_0^H \rho_{step} gz \, dz = \int_0^{H/2} \rho_1 gz \, dz + \int_{H/2}^H \rho_2 gz \, dz. \tag{44}$$

Also, at $T = 0$, $KE_i \sim 0$, since there is negligible energy associated with velocity fluctuations. Further downstream, the potential energy at $T = 1.21$ is computed from the measured density profile as

$$PE_f = \int_0^H \rho_{measured} g z \, \mathrm{d}z \cong \sum_{i=0}^{n} \rho_i g z_i \Delta z. \tag{45}$$

The potential energy released to the flow by $T = 1.21$ is then given by $PE_{released} = PE_f - PE_i$. Some of this energy is converted into kinetic energy, which can be directly obtained from our measured velocity profiles of u' and v'. As previously mentioned, observations of the axisymmetric mushroom structures mean we may take the turbulence as homogeneous with respect to the streamwise direction x and the spanwise direction z, and set $\langle u'^2 \rangle = \langle w'^2 \rangle$. Then,

$$KE_{generated} = \tfrac{1}{2} \int_0^H \rho (2\langle u'^2 \rangle + \langle v'^2 \rangle) \, \mathrm{d}z, \tag{46}$$

and the net kinetic energy dissipation is given by

$$D = PE_{released} - KE_{generated}. \tag{47}$$

The net KE dissipation as a fraction of the potential energy released, $D/PE_{released}$ was determined from our measurements to be 0.49 at $T \sim 1.21$. Youngs (1994) reported a value of 0.52 obtained from three-dimensional numerical simulations, and significantly lesser values from two-dimensional simulations ($D/PE_{released} \sim 0.06$) since dissipation is primarily a three-dimensional mechanism. For a self-similar mix, characterized by the length scale gt^2, it is expected that $D/PE_{released}$ and $KE_{generated}/PE_{released}$ become constant in the self-similar regime. Thus, we find good agreement between the present experiments and related, but higher Atwood number, three-dimensional simulations.

6. Conclusions

The evolution of small-Atwood-number ($< 10^{-3}$) Rayleigh–Taylor (R-T) mixing into self-similar turbulence has been studied through high-resolution temperature and velocity measurements. The velocity measurements were obtained from the particle image velocimetry technique, while temperature measurements were made using a rake of E-type thermocouples placed across the mix. In addition, using the PIV-S technique, simultaneous measurements of velocity and density fields have been obtained.

In this experiment, the R-T mix is initialized with a spectrum of velocity perturbations that, after a stage of linear growth, evolve through mode-interactions and successive wavelength saturation. The fully developed mix grows quadratically in time, with a self-similar structure. The self-similarity is evident here through velocity and density frequency spectra that evolve in a shape-preserving manner. The velocity profiles also collapse onto a single curve when normalized by suitable similarity variables. The mix width development was characterized using centreline vertical velocity fluctuations, rather than the mix width itself. The quadratic growth rate constant α was measured at 0.07, which is in good agreement with previous measurements from the experiment using the mix width based on the 5% and 95% threshold for the volume fractions. This verifies observations, and results from velocity and density spectra, that large-scale structures dominate the mixing and contain most of the kinetic energy of the mix. It also implies that relatively simple models, based on driven centreline velocity fluctuations and density fluctuations, would suffice to capture the overall development of the mix.

The internal structure of the self-similar mix is anisotropic with vertical velocity fluctuations dominating the horizontal (streamwise and transverse) components. The ratio of v'/u' is ~ 2, and appears to be constant across the mix, as the mushroom-shaped structures are convected up and down the mix without much change in shape. This significant cross-stream flux limits the intermittency factor (based on a vorticity threshold) to a maximum of 0.5 at the centre of the mix, as opposed to a value of 1 for shear layers. A more natural definition for intermittency for buoyancy-driven turbulence is suggested here based on the two-fluid density fluctuation B_2 and takes a value of 0.5 at the centreline.

The anisotropy of fluctuating velocity components extends to the Taylor scales, which also exhibit a preferential straining in the direction of gravity. It might be expected that at scales smaller than this, as we approach the Kolmogorov dimensions, the turbulence would be far more isotropic. However, this cannot be directly verified here owing to the limitation on spatial resolution of our PIV system. The velocity spectra show a tendency toward convergence at high wavenumbers. This trend is also seen in the strain rate spectrum, which shows that, under the influence of an imposed strain field, the highest wavenumbers take the least time to return to an isotropic configuration.

The R-T flow may be viewed as a mixing process for miscible/immiscible fluids of different densities. From an energy budget analysis, it was shown that there is considerable kinetic energy dissipation ($\sim 50\%$ of the potential energy loss), which indicates the presence of highly three-dimensional structures necessary for mixing to occur. The molecular mix fraction, a local mix parameter, was determined to be ~ 0.75 in the self-similar region.

We close by suggesting that the spectral and statistical data presented here may be used to validate direct numerical simulations and turbulence models such as the Reynolds stress models, spectral transport model and two-fluid models of R-T mixing.

This material is based upon work that was supported by the US Department of Energy under contract numbers DE-FG03-99DP00276/A000 and DE-FG03-02NA00060. The authors would like to thank Wayne Kraft for his help in performing the laser induced fluorescence experiments.

REFERENCES

Adrian, R. J. 1991 Particle-imaging techniques for experimental fluid mechanics. *Annu. Rev. Fluid Mech.* **23**, 261–304.

Adrian, R. J. 1997 Dynamic ranges of velocity and spatial resolution of particle image velocimetry. *Meas. Sci. Technol.* **8**, 1393–1398.

Andrews, M. J. 1986 Turbulent mixing by Rayleigh–Taylor instability. PhD dissertation, London University.

Andrews, M. J. & Spalding, D. B. 1990 A simple experiment to investigate two-dimensional mixing by Rayleigh–Taylor instability. *Phys. Fluids* A **2**, 922–927.

Beale, J. C. & Reitz, R. D. 1999 Modeling spray atomization with Kelvin–Helmholtz/Rayleigh–Taylor hybrid model. *Atomiz. Sprays* **9**, 623–650.

Besnard, D., Harlow, F. H., Rauenzahn, R. & Zemach, C. 1990 Spectral transport model for turbulence. *Los Alamos Rep.* LA-11821.

Besnard, D., Harlow, F. H., Rauenzahn, R. & Zemach, C. 1992 Turbulence transport equations for variable density turbulence, and a relationship to two-fluid models. *Los Alamos Rep.* LA-11303.

Chandrasekhar, S. 1961 *Hydrodynamic and Hydromagnetic Stability*. Clarendon.

Cook, A. W. & Dimotakis, P. E. 2001 Transition stages of Rayleigh–Taylor instability between miscible fluids. *J. Fluid Mech.* **443**, 69–99.

Cook, A. W. & Zhou, Y. 2002 Energy transfer in Rayleigh–Taylor instability. *Phys. Rev.* E **66**, 026312.

Corrsin, S. 1951 On the spectrum of isotropic temperature fluctuations in an isotropic turbulence. *J. Appl. Phys.* **22**, 469–473.

Daly, B. J. 1967 Numerical study of two fluid Rayleigh–Taylor instability. *Phys. Fluids* **10**, 297–307.

Dalziel, S. B. 1993 Rayleigh–Taylor instability: experiments with image analysis. *Dyn. Atmos. Oceans* **20**, 127–153.

Dalziel, S. B., Linden, P. F. & Youngs, D. L. 1999 Self-similarity and internal structure of turbulence induced by Rayleigh–Taylor instability. *J. Fluid Mech.* **399**, 1–48.

Dankwerts, P. V. 1952 The definition and measurement of some characteristics of mixtures. *Appl. Sci. Res.* **3**, 279–296.

Dimonte, G. 2004 Dependence of turbulent Rayleigh–Taylor (RT) instability on initial conditions. Phys. Rev. E (to appear).

Dimonte, G. & Schneider, M. 1996 Turbulent Rayleigh–Taylor instability experiments with variable acceleration. *Phys. Rev.* E **54**, 3740–3743.

Dimonte, G. & Schneider, M. 2000 Density ratio dependence of Rayleigh–Taylor mixing for sustained and impulsive acceleration histories. *Phys. Fluids* **12**, 304–321.

Dimonte, G., Youngs, D. L., Dimits, A. *et al.* 2004 A comparative study of the turbulent Rayleigh–Taylor (RT) instability using high-resolution 3D numerical simulations: The Alpha-Group collaboration. *Phys. Fluids* (to appear).

Dimotakis, P. E. 2000 The mixing transition in turbulent flows. *J. Fluid Mech.* **409**, 69–98.

Emmons, H. W., Chang, C. T. & Watson, B. C. 1960 Taylor instability of finite surface waves. *J. Fluid Mech.* **7**, 177–193.

Glimm, J., Grove, J. W., Li, X. L., Oh., W. & Sharp, D. H. 2001 A critical analysis of Rayleigh–Taylor growth rates. *J. Comput. Phys.* **169**, 652–677.

Grue, J., Jensen, A., Rusas, P. & Sveen, J. K. 2000 Breaking and broadening of internal solitary waves. *J. Fluid Mech.* **413**, 181–217.

Gull, S. F. 1975 The X-ray, optical and radio properties of young supernova remnants. *Mon. Not. R. Astr. Soc.* **171**, 263–278.

Jaffe, N. A., Okamura, T. T. & Smith, M. O. 1970 Determination of spatial amplification factors and their application to predicting transition. *AIAA J.* **8**, 301–308.

Jevons, W. S. 1857 On the cirrus formation of cloud. *Phil. Mag.* **14** (90), 22–35.

Kukulka, D. J. 1981 Thermodynamic and transport properties of pure and saline water. MS dissertation, State University of New York at Buffalo.

LaRue, J. C. & Libby, P. A. 1976 Statistical properties of the interface in the turbulent wake of a heated cylinder. *Phys. Fluids* **19**, 1864–1975.

Lawrence, G. A., Browand, F. K. & Redekopp, L. G. 1991 The stability of a sheared density interface. *Phys. Fluids.* A **3**, 2360–2370.

Layzer, D. 1955 On the instability of superposed fluids in a gravitational field. *Astrophys. J.* **122**, 1–12.

Lewis, D. J. 1950 The instability of liquid surfaces when accelerated in a direction perpendicular to their planes II. *Proc. R. Soc. Lond.* A **202**, 81–96.

Linden, P. F., Redondo, J. M. & Youngs, D. I. 1994 Molecular mixing in Rayleigh–Taylor instability. *J. Fluid Mech.* **265**, 97–124.

Lindl, J. D. 1998 *Inertial Confinement Fusion: The Quest for Ignition and Energy Gain Using Indirect Drive.* AIP Press.

Nelder, J. A. & Mead, R. 1965 A Simplex method for function minimization. *Comput. J.* **7**, 308–313.

Obukhov, A. M. 1949 Structure of the temperature field in turbulent flows. *Izv. Akad. Nauk SSSR, Geogr. Geopphys.* **13**, 58–69.

Pope, S. B. 2000 *Turbulent Flows.* Cambridge University Press.

Prestridge, K., Rightley, P. M., Vorobieff, P., Benjamin, R. F. & Kurnit, N. A. 2000 Simultaneous density-field visualization and PIV of a shock-accelerated gas curtain. *Exps. Fluids* **29**, 339–347.

Ramaprabhu, P. 2003 On the dynamics of Rayleigh–Taylor mixing. PhD dissertation, Texas A&M University.

Ramaprabhu, P. & Andrews, M. J. 2003 Simultaneous measurements of velocity and density in buoyancy-driven mixing. *Exps. Fluids* **34**, 98–106.

Ratafia, M. 1973 Experimental investigation of Rayleigh–Taylor instability. *Phys. Fluids* **16**, 1207–1210.

Read, K. I. 1984 Experimental investigation of turbulent mixing by Rayleigh–Taylor instability. *Physica* D **12**, 45–58.

Scarano, F. & Riethmuller, M. L. 1999 Iterative multigrid approach in PIV image processing with discrete window offset. *Exps. Fluids* **26**, 513–523.

Snider, D. M. & Andrews, M. J. 1994 Rayleigh–Taylor and shear driven mixing with an unstable thermal stratification. *Phys. Fluids* A **6**, 3324–3334.

Snider, D. M. & Andrews, M. J. 1996 The simulation of mixing layers driven by compound buoyancy and shear. *J. Fluids Engng* **118**, 370–376.

Steinkamp, M. J. 1995 Spectral analysis of the turbulent mixing of two-fluids. PhD thesis, University of Illinois at Urbana-Champaign.

Steinkamp, M. J., Clark, T. & Harlow, F. H. 1995 Stochastic interpenetration of fluids. *Los Alamos Rep.* LA-131016.

Stewart, R. W. 1968 Turbulence. Color-no. 21626 (distributed by Encyclopaedia Britannica Educational Corporation, 310 South Michigan Avenue, Chicago, Illinois 60604, USA).

Tennekes, H. & Lumley, J. L. 1972 *A First Course in Turbulence*. MIT Press.

Turner, J. S. 1980 *Buoyancy Effects in Fluids*. Cambridge University Press.

Waddell, J. T., Niederhaus, C. E. & Jacobs, J. W. 2001 Experimental study of Rayleigh–Taylor instability: low Atwood number liquid systems with single-mode initial perturbations. *Phys. Fluids* **13**, 1263–1273.

Wilson, P. N. & Andrews, M. J. 2002 Spectral measurements of Rayleigh–Taylor mixing at low-Atwood number. *Phys. Fluids* A **14**, 938–945.

Wilson, P., Andrews, M. & Harlow F. 1999 Spectral nonequilibrium in a turbulent mixing layer. *Phys. Fluids* A **11**, 2425–2433.

Youngs, D. L. 1984 Numerical simulation of turbulent mixing by Rayleigh–Taylor instability. *Physica* D **12**, 32–44.

Youngs, D. L. 1989 Modeling turbulent mixing by Rayleigh–Taylor instability. *Physica* D **37**, 270–287.

Youngs, D. L. 1994 Numerical simulation of Rayleigh–Taylor and Richtmeyer–Meshkov instabilities. *Lasers Part. Beams* **12**, 725–750.

Youngs, D. L. 2003 Application of MILE to Rayleigh–Taylor and Richtmeyer–Meshkov mixing. *16th AIAA Computational Fluid Dyn. Conf. 23–26 June 2003 AIAA*, p. 4102.

Young, Y. N., Tufo, H., Dubey, A. & Rosner, R. 2001 On the miscible Rayleigh–Taylor instability: two and three dimensions. *J. Fluid Mech.* **447**, 377–408.

Zhou, Y. 2001 A scaling analysis of turbulent flows driven by Rayleigh–Taylor and Richtmeyer–Meshkov instabilities. *Phys. Fluids* **13**, 538–543.